

# Elliptical pore regularisation of the inverse problem for microstructured optical fibre fabrication

Peter Buchak<sup>1,†</sup>, Darren G. Crowdy<sup>1</sup>, Yvonne M. Stokes<sup>2</sup> and Heike Ebendorff-Heidepriem<sup>3</sup>

<sup>1</sup>Department of Mathematics, Imperial College London, 180 Queen's Gate, London SW7 2AZ, UK

<sup>2</sup>School of Mathematical Sciences, The University of Adelaide, North Terrace, Adelaide, SA 5005, Australia

<sup>3</sup>ARC Centre of Excellence for Nanoscale BioPhotonics, Institute for Photonics and Advanced Sensing, School of Chemistry and Physics, The University of Adelaide, North Terrace, Adelaide, SA 5005, Australia

(Received 18 July 2014; revised 22 January 2015; accepted 15 June 2015;  
first published online 30 July 2015)

A mathematical model is presented describing the deformation, under the combined effects of surface tension and draw tension, of an array of channels in the drawing of a broad class of slender viscous fibres. The process is relevant to the fabrication of microstructured optical fibres, also known as MOFs or holey fibres, where the pattern of channels in the fibre plays a crucial role in guiding light along it. Our model makes use of two asymptotic approximations, that the fibre is slender and that the cross-section of the fibre is a circular disc with well-separated elliptical channels that are not too close to the outer boundary. The latter assumption allows us to make use of a suitably generalised ‘elliptical pore model (EPM)’ introduced previously by one of the authors (Crowdy, *J. Fluid Mech.*, vol. 501, 2004, pp. 251–277) to quantify the axial variation of the geometry during a steady-state draw. The accuracy of the elliptical pore model as an approximation is tested by comparison with full numerical simulations. Our model provides a fast and accurate reduction of the full free-boundary problem to a coupled system of nonlinear ordinary differential equations. More significantly, it also allows a regularisation of an important ill-posed inverse problem in MOF fabrication: how to find the initial preform geometry and the experimental parameters required to draw MOFs with desired cross-plane geometries.

**Key words:** interfacial flows (free surface), low-Reynolds-number flows, lubrication theory

## 1. Introduction

The fabrication of a microstructured optical fibre, or MOF, typically involves the drawing down of a preform comprising a cylinder of glass or polymer 1–3 cm in diameter containing a pattern of axial channels running through its length, usually 10–30 cm. The preform is held at one end in a movable clamp at the top of a draw tower and fed downwards through a heated zone in which the glass softens so that it

† Email address for correspondence: [p.buchak@imperial.ac.uk](mailto:p.buchak@imperial.ac.uk)

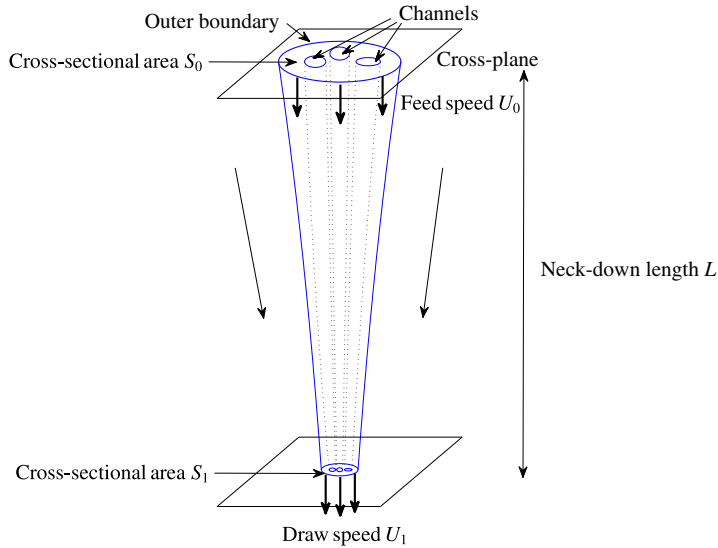


FIGURE 1. (Colour online) Schematic of the drawing of a multichannel MOF: a preform with cross-sectional area  $S_0$  containing multiple channels is fed into a hot zone at speed  $U_0$  and pulled down at a draw speed  $U_1$  to a cross-sectional area  $S_1$  over a ‘neck-down length’  $L$ . During the draw, the channel shapes deform due to a combination of surface tension and draw tension.

can be drawn from below at a speed typically much larger than the feed speed. At the base of the draw tower the (now cool) fibre is wound around a rotating drum so that it can be conveniently stored for future use. The draw process through the neck-down length is depicted in figure 1.

Both the draw ratio – the ratio of the draw speed to the feed speed – and the temperature are important control parameters. The draw ratio determines the reduction in the area of the cross-section as it travels along the ‘neck-down length’ of several centimetres (typically of the same order as the heated zone length). To obtain a fibre having a typical diameter of 100–200  $\mu\text{m}$  from a preform with a diameter of a centimetre, the draw ratio will typically be in excess of 4000. Large draw ratios of up to 10 000 are common in practical fibre drawing, without the onset of draw-resonance instability as predicted by linear stability analyses at draw ratios in excess of a little over 20 (Pearson & Matovich 1969; Yarin, Gospodinov & Roussinov 1994; Fitt *et al.* 2002), with control of fibre tension, cooling of the fibre and, perhaps, other factors having a stabilising effect (Pearson & Matovich 1969; Gospodinov & Yarin 1997; Scheid *et al.* 2010). The temperature determines the material viscosity and, in turn, the fibre tension, which must be within an appropriate range – too small and its diameter will be difficult to control, too large and the fibre will break. In this paper the effect of gravity is assumed to be small and is neglected.

For microstructured optical fibres of interest in applications, there is a large variation in the number of channels, from just a few to perhaps 100 or more. However, the number of channels is not necessarily large, which renders the proposition of a mean-field model of the cross-plane structure unlikely to be useful in practice. Moreover, it has been observed that the shapes of some channels are deformed more than others during the drawing process, implying that detailed resolution of

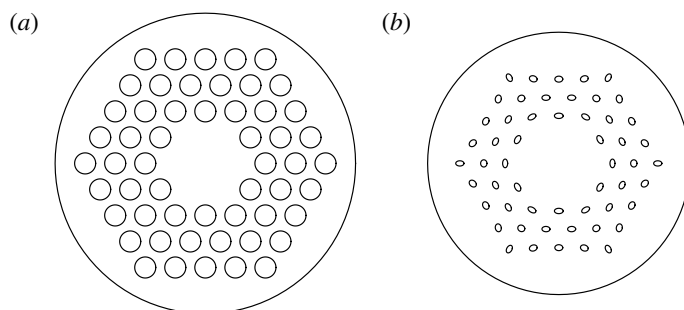


FIGURE 2. Typical deformations of non-pressurised circular channels in a microstructured optical fibre due to surface tension effects, calculated using the model described in §5. Circular channels (a) deform to approximately elliptical channels (b), with the degree and nature of the deformation being dependent upon relative position. Such deformations must be controlled in the fabrication process.

the evolution of the cross-plane geometry is needed, along with an understanding of how this evolution is affected by different experimental conditions. Figure 2 shows typical shape deformations, due to surface tension effects, of an arrangement of initially circular channels of equal size. A key observation is that they deform to approximately elliptical channels, with the degree and nature of the deformation being dependent upon relative position in the array: channels in the inner ring are drawn out in the azimuthal direction, while those in the outer ring tend to be extended radially; similar deformations can be seen in the image in figure 1 of Issa *et al.* (2004). Because even minor unwanted deformations in a small number of the channels can severely compromise a fibre's optical performance, it is highly desirable to gain an improved understanding of the channel deformations. A good survey of the applications and fabrication challenges associated with MOFs can be found in Lyytikäinen (2004).

One attempt to predict experimentally relevant parameters from a mathematical model has recently been made (Kostecki *et al.* 2014). The idea of that model is to approximate a non-trivial MOF geometry comprising several channels with an 'effective' capillary tube geometry with just a single channel so that the mathematical model of the drawing of an axisymmetric tube presented by Fitt *et al.* (2002) can be used. The challenge then becomes one of finding the best way to approximate the radius of this capillary for some given MOF cross-sectional geometry. The approach is found to give good estimates for the required experimental draw parameters for geometries of a few channels. However, it does not resolve details of the shape deformations under the draw and may not be generalisable to fibres having many channels.

The aim of this paper is to present an improved model which captures the free-boundary evolution for multichannel fibres in more detail. Our model provides valuable insights into how experimental variables such as fluid viscosity (controlled, as mentioned above, by varying the glass temperature), feed and draw speeds as well as surface tension affect the shape of the channels during the draw. For a given preform shape and given draw parameters, the model provides predictions of how the channels will deform. Conversely, it turns out that we can also use the model to provide solutions to the inverse problem – designing a suitable preform shape which, under given experimental conditions, will produce the desired fibre geometry.

The key theoretical tool employed here is to adapt, to the cross-plane problem in fibre drawing, a so-called ‘elliptical pore model’ (or EPM, for short) devised by one of the authors (Crowdy 2004) to model the dynamics of a finite set of interacting compressible two-dimensional bubbles in Stokes flow. By combining this simplified asymptotic model of the evolution of interacting channels in the cross-plane with a different asymptotic approximation based on the slenderness of the fibres in the axial direction, a powerful reduction of the full three-dimensional free-boundary problem is achieved. Here, we test the effectiveness of this scheme by comparison with full numerical simulations of the cross-plane evolution, and examine its implications for practical fibre drawing. Moreover, it turns out that the EPM affords a second advantage in regularising the inverse problem of finding a suitable initial preform geometry which, at the end of a draw, will deliver the required target fibre geometry.

In a more general set-up, differential pressurisation of the individual channels is also used as a control device during the draw. However, precisely how such pressures should be chosen to achieve a desired target is not fully understood, and at present pressurisation is implemented largely on a trial-and-error basis. Channel pressurisation is used both to prevent channels from closing up and also as a direct means to expand the channel cross-sectional areas if it proves impossible, or inconvenient, to manufacture an initial preform with channels of the appropriate size. Pressurisation is usually necessary when the cross-sectional profile comprises thin bridges of glass, since there are practical and mechanical limitations to the successful fabrication of suitable preforms in such cases.

For now, however, we focus on an important baseline case where the gas pressure in each channel is equal to the ambient pressure. Moreover, we take the fluid viscosity to be constant everywhere. The assumption of constant viscosity makes the derivation simpler and is not a serious restriction. One could solve for a variable viscosity by coupling the flow model with an equation for energy balance, as done by Yarin *et al.* (1989), Griffiths & Howell (2008) and Taroni *et al.* (2013). However, in Stokes, Buchak & Crowdy (2014), we show that for known fibre tension and draw ratio, knowledge of an axially varying viscosity is unnecessary for determining the final geometry from a fibre draw, so an effective constant viscosity may be assumed. Our model is also extendable to differentially pressurised channels; our investigation of this will be published elsewhere.

## 2. The free-boundary problem

The following general set-up closely follows that described by Stokes *et al.* (2014). A preform with cross-sectional area  $S_0$  containing  $M \geq 1$  channels is fed vertically down into a hot zone at speed  $U_0$  and pulled down at a draw speed  $U_1$  to a cross-sectional area  $S_1$  over a ‘neck-down length’  $L$ . The shapes of the channels deform during the draw due to the combined effects of surface tension and draw tension. A schematic of the drawing of such a fibre is shown in figure 1. The  $x$ -axis is directed vertically down along the axis of the fibre.

As shown in Stokes *et al.* (2014), neglect of inertia is justified because the Reynolds number typical for fibre drawing is very small,  $O(10^{-8})$ . We also neglect gravity. Thus, the material making up the preform is assumed to be a viscous Newtonian fluid in the Stokes regime, and its incompressible velocity field  $\mathbf{u}$  satisfies

$$-\nabla p + \mu \nabla^2 \mathbf{u} = 0, \quad \nabla \cdot \mathbf{u} = 0, \quad (2.1a,b)$$

where  $p$  is the pressure in the fluid and  $\mu$  is its viscosity, here assumed to be constant and uniform throughout the fluid. The fluid has  $M + 1$  free surfaces, one for each of

the  $M$  channels, together with an outer boundary. Using  $k=0$  for the outer boundary and  $k=1, \dots, M$  for the  $k$ th channel, the dynamic boundary condition on the  $k$ th free surface is

$$\sigma_{ij}n_j = -\gamma\kappa n_i - p_B^{(k)} n_i, \tag{2.2}$$

where  $\kappa$  is the surface curvature,  $\gamma$  is the surface tension,  $\sigma_{ij}$  is the fluid stress tensor and  $p_B^{(k)}(t)$  is the pressure on the  $k$ th boundary. Without loss of generality, we set  $p_B^{(0)} = 0$ . Under the assumption of quasi-steady flow, the normal velocity  $V_k$  of each boundary point is given by

$$V_k = \mathbf{u} \cdot \mathbf{n}. \tag{2.3}$$

In addition, the boundary conditions at  $x = 0$  and  $x = L$  are  $\mathbf{u} = U_0\mathbf{i}$  and  $\mathbf{u} = U_1\mathbf{i}$  respectively.

Following Cummings & Howell (1999), we introduce a small parameter  $\epsilon$  characterising the slenderness of the fibre,

$$\epsilon = \frac{\sqrt{S_0}}{L} \ll 1, \tag{2.4}$$

which is found to be well satisfied for fibres typically encountered in practice. We also define the dimensionless surface tension  $\gamma^*$  in terms of the physical parameters of the problem,

$$\gamma^* = \frac{\gamma L}{\mu\sqrt{S_0}U_0}. \tag{2.5}$$

Cummings & Howell (1999) showed that for a slender fibre ( $\epsilon \ll 1$ ), the three-dimensional problem splits into two simpler problems: a one-dimensional problem in the axial (i.e.  $x$ ) direction ('stretching') and a two-dimensional problem in the cross-plane ('sintering'). The cross-plane problem turns out to be simply the classical two-dimensional problem of surface-tension-driven Stokes flow with unit cross-sectional area, surface tension and viscosity, evolving with respect to a reduced time variable  $\tau$  to be introduced shortly.

The stretching problem is governed by a pair of differential equations in the axial coordinate  $x$  and time  $t$ . Generalisation of the derivation of Cummings & Howell (1999) to allow for the presence of pressurised channels, conservation of mass and momentum in each cross-section requires respectively

$$S_t + (uS)_x = 0, \tag{2.6}$$

$$3(Su_x)_x + \frac{1}{2}\gamma^* \sum_{k=0}^M (\Gamma_k)_x = \sum_{k=0}^M \pm (p_B^{(k)})_x \mathcal{A}_k. \tag{2.7}$$

Here,  $S(x, t)$  is the cross-sectional area of the fluid region,  $u(x, t)$  is the axial fluid velocity, and  $\mathcal{A}_k(x, t)$ ,  $\Gamma_k(x, t)$  and  $p_B^{(k)}(x, t)$  are the area, perimeter and pressure associated with the  $k$ th boundary. Introducing Lagrangian coordinates  $\tilde{x}$  and  $\tilde{t}$ ,

$$t = \tilde{t}, \quad x = \int_0^{\tilde{t}} u(\tilde{x}, T) dT + \tilde{x}, \tag{2.8}$$

the reduced time  $\tau$  is defined by (Cummings & Howell 1999; Griffiths & Howell 2008)

$$\tau = \gamma^* \int_0^{\tilde{t}} \frac{d\tilde{t}}{\sqrt{S}}. \tag{2.9}$$

In steady fibre drawing, this reduced time  $\tau$  characterising the cross-plane evolution is related to the  $x$  coordinate by

$$\frac{\partial x}{\partial \tau} = \frac{u\sqrt{S}}{\gamma^*}. \tag{2.10}$$

In (2.6)–(2.10), distances in the axial direction have been scaled by  $L$ , distances in the cross-plane have been scaled by  $\sqrt{S_0}$ , the axial velocity has been scaled by  $U_0$ , and time and pressure have been scaled by  $L/U_0$  and  $\mu U_0/L$  respectively.

In the next section we summarise results from a companion paper (Stokes *et al.* 2014), where it is demonstrated that the solution to the axial problem for arbitrary cross-plane geometries can be given in terms of explicit formulae. It should be noted that the formulation of Stokes *et al.* (2014) allows for an axially varying viscosity profile, while here we focus on the case where the fluid viscosity is uniform. Should it be desirable to consider a non-constant viscosity, the required modifications to the model are as in Stokes *et al.* (2014).

### 3. Explicit formulae for stretching and model predictions

In this section, we focus on the special case in which none of the channels are pressurised relative to the ambient pressure, therefore

$$p_B^{(k)}(x, t) = 0, \quad k = 0, 1, \dots, M. \tag{3.1}$$

In steady fibre drawing, it is expedient (Stokes *et al.* 2014) to introduce an important function

$$H(\tau) = \exp\left(-\frac{1}{12} \int_0^\tau \tilde{\Gamma}(\tau') \, d\tau'\right), \tag{3.2}$$

where  $\tilde{\Gamma}(\tau)$  is the total boundary perimeter in the cross-plane, scaled by  $\sqrt{S_0 S(\tau)}$ . The total boundary perimeter  $\tilde{\Gamma}(\tau)$  can be readily computed as the sum of the perimeters of the individual boundaries once the solution for the cross-plane problem, with total area normalised to be unity, has been found. With  $H(\tau)$  known from (3.2), for a fluid with constant uniform viscosity the cross-section  $S(\tau)$  and axial position  $x(\tau)$  are given explicitly as

$$S(\tau) = \left(1 - \frac{\sigma^*}{\gamma^*} \int_0^\tau H(\tau') \, d\tau'\right)^2 / H(\tau)^2, \tag{3.3}$$

$$x(\tau) = -\frac{1}{\sigma^*} \log(H(\tau)\sqrt{S(\tau)}). \tag{3.4}$$

The parameter  $\sigma^*$  is the scaled fibre tension related to the physical tension  $\sigma$  by

$$\sigma = \frac{6\mu U_0 S_0}{L} \sigma^*. \tag{3.5}$$

Formulae (3.3) and (3.4) give the complete solution, parametrised by  $\tau$ , to the three-dimensional fibre drawing problem from a solution of the cross-plane problem.

It is interesting to point out that, in devising a scheme to apply the predictions of the model described in Fitt *et al.* (2002) for the pulling of a capillary tube – that is, a fibre with just one central channel – to the drawing of MOFs with several channels, KostECKI *et al.* (2014) were compelled to study the multichannel geometry

to find some quantity that best approximates the single internal channel radius appearing in the equations of the Fitt model. They found that, among several other apparently reasonable options, the best choice is to use the total perimeter length of the collection of channels in the MOF cross-plane. Intuitively, this empirical observation is consonant with the fact that the total cross-plane perimeter plays a crucial role in our own formulation just described.

According to the approach advocated by Stokes *et al.* (2014),  $\tau = 0$  labels the initial channel configuration, and one chooses the value  $\tau = \tau_L$  corresponding to the desired fibre configuration. In this way  $\tau_L$  is the duration of the ‘sintering’ process. By  $\tau = \tau_L$ , the cross-section must reach the scaled axial distance to the end of the draw,  $x = 1$ , and the axial fluid velocity must reach the specified scaled draw speed,  $u = U_1/U_0 = D$ , where  $D$  is the draw ratio. These boundary conditions give two constraints on the four parameters  $\tau_L$ ,  $\gamma^*$ ,  $D$  and  $\sigma^*$ ,

$$\sigma^* = \log \left( \frac{\sqrt{D}}{H(\tau_L)} \right), \quad \frac{H(\tau_L)}{\sqrt{D}} = 1 - \frac{\sigma^*}{\gamma^*} \int_0^{\tau_L} H(\tau') d\tau'. \quad (3.6a,b)$$

From (2.5) and (3.5), the ratio of the dimensionless parameters  $\gamma^*$  and  $\sigma^*$  is related to the ratio of the physical tensions  $\gamma$  and  $\sigma$  by

$$\frac{\sigma}{\gamma} = 6\sqrt{S_0} \frac{\sigma^*}{\gamma^*}. \quad (3.7)$$

As discussed in Stokes *et al.* (2014), this is an important result. For drawing of a particular fibre from a given preform,  $\tau_L$  and  $D$  are known, and since the physical surface tension  $\gamma$  can be considered to be known *a priori*, (3.6b) and (3.7) can be solved for the required physical fibre tension  $\sigma$ . Conversely, when  $D$  and  $\sigma$  are measured, (3.6b) and (3.7) can be solved for  $\tau_L$ , which gives the final fibre geometry. Thus, use of the measurable and controllable physical fibre tension  $\sigma$  circumvents the need for specific knowledge of the unknown fluid viscosity  $\mu$  and neck-down length  $L$  for the draw, both of which can vary with the draw parameters. This was also noted by Chen & Birks (2013).

If desired, the ratio  $\mu/L$  can be computed by combining (3.5) and (3.6a). Further, an estimate of the fluid viscosity  $\mu$  can be obtained if, as done by previous authors (Fitt *et al.* 2002), the neck-down length  $L$  is assumed to be equal to the length of the heated zone. This assumption then permits the physical geometry to be determined over the neck-down length. However, we emphasise that it is usually the final geometry that is of interest rather than the geometry throughout the neck-down zone, so that  $\gamma^*$  and  $\sigma^*$  need not be computed separately, and there is no need to know or determine the viscosity  $\mu$  or to make any assumptions about the neck-down length  $L$ . The slightly more complex case of axially varying viscosity is considered in Stokes *et al.* (2014), leading to the same result for any viscosity profile.

The conditions (3.6a,b) may be written more succinctly (Stokes *et al.* 2014) as the single constraint

$$\frac{1}{\mathcal{Q}} + \frac{\log \mathcal{Q}}{\mathcal{P}} = 1, \quad (3.8)$$

where

$$\mathcal{P} = \frac{\gamma^*}{\int_0^{\tau_L} H(\tau') d\tau'}, \quad \mathcal{Q} = \frac{\sqrt{D}}{H(\tau_L)}. \quad (3.9a,b)$$

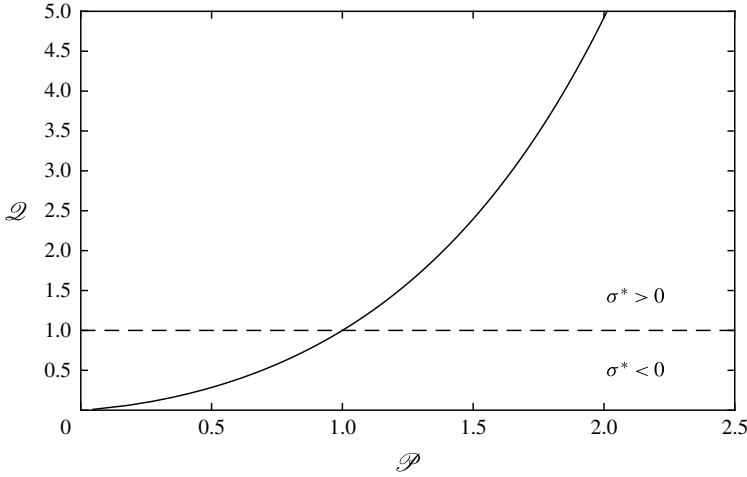


FIGURE 3. The balance of tensions as given by the curve (3.8). The region  $\mathcal{Q} > 1$  corresponds to positive draw tension. Increasing  $\mathcal{P}$ , and hence surface tension so that the cross-plane deformations happen over a shorter time scale, requires a higher  $\mathcal{Q}$  (essentially, draw ratio) to achieve the same target geometry.

The choice of  $\tau_L$  picks out the final geometry and, in turn, gives the denominators in the definitions (3.9) of  $\mathcal{P}$  and  $\mathcal{Q}$ . The variable  $\mathcal{P}$  gives a measure of the surface tension while  $\mathcal{Q} = \exp(\sigma^*)$  is a measure of the draw tension.

Formula (3.8) represents the balance between draw tension and surface tension required to achieve a desired geometry in a constant-viscosity fluid with no channel pressurisation. A graph of  $\mathcal{Q}$  against  $\mathcal{P}$  is shown in figure 3. From it we learn that small changes in  $\mathcal{P}$  (surface tension) can lead to large corresponding changes in  $\mathcal{Q}$ , and hence draw ratio  $D$ , for the same desired final configuration. The logarithmic dependence of draw tension  $\sigma^*$  on  $\mathcal{Q}$  means, however, that the corresponding change in draw tension is less sensitive to changes in  $\mathcal{P}$ .

#### 4. The cross-plane problem

To model the drawing of MOFs of general shape it is necessary to solve for the evolution of a given cross-plane geometry evolving under the effect of surface tension. We now briefly describe the free-boundary cross-plane problem and the formulation of a numerical method that we have devised for its solution. This numerical method is interesting in itself and will be described in detail elsewhere (Buchak & Crowdy 2014). Its main use for the present purposes is simply to test the accuracy of an approximate (elliptical pore) model to be presented in §5. A boundary integral approach to the same numerical problem has been proposed by Chakravarthy & Chiu (2009), but it differs in several respects from the approach adopted here.

The cross-plane problem for steady fibre drawing is governed by the Stokes equations,

$$-\nabla p + \mu \nabla^2 \mathbf{u} = 0, \quad \nabla \cdot \mathbf{u} = 0, \tag{4.1a,b}$$

with boundary conditions

$$\sigma_{ij} n_j = -\gamma \kappa n_i - p_B^{(n)} n_i, \quad V_n = \mathbf{u} \cdot \mathbf{n}, \tag{4.2a,b}$$



where now the flow is two-dimensional and the boundaries are closed curves in the cross-plane. Lengths are scaled by  $\sqrt{S_0 S(\tau)}$ , velocities by  $\sqrt{S_0} U_0 \gamma^* / L$  and pressures by  $\mu U_0 \gamma^* / L \sqrt{S(\tau)}$ . The fluid region evolves in the reduced time  $\tau$  defined in (2.9) and has unit area, unit surface tension and unit viscosity (our numerical method can be applied to more general two-dimensional Stokes flow, so for this reason we retain the constants  $\mu$  and  $\gamma$  in the following description).

Two-dimensional incompressible flow can be formulated in terms of a streamfunction  $\psi(x, y)$ , satisfying

$$\nabla^4 \psi = 0, \tag{4.3}$$

where  $\nabla^2$  denotes the two-dimensional Laplacian operator in the cross-plane. Introducing the complex variable  $z$  as the cross-plane coordinate in the usual way, the general solution to (4.3) can be written

$$\psi = \text{Im}[\bar{z}f(z, \tau) + g(z, \tau)], \tag{4.4}$$

where  $f(z, \tau)$  and  $g(z, \tau)$  are two functions analytic in the fluid. The fluid velocity  $(u, v)$ , vorticity  $\omega$ , pressure  $p$  and rate-of-strain tensor  $e_{ij}$  are given by (Langlois 1964; Crowdy 2003a)

$$\frac{p}{\mu} - i\omega = 4f'(z, \tau), \tag{4.5}$$

$$u + iv = -f(z, \tau) + \overline{zf'(z, \tau)} + \overline{g'(z, \tau)}, \tag{4.6}$$

$$e_{11} + ie_{12} = \overline{zf''(z, \tau)} + \overline{g''(z, \tau)}. \tag{4.7}$$

From these results it can be shown that the boundary conditions (4.2) on each boundary  $n$  ( $n = 0, \dots, M$ ) are

$$f(z, \tau) + \overline{zf'(z, \tau)} + \overline{g'(z, \tau)} = -\frac{1}{2}i\gamma z_s + \frac{1}{2}p_B^{(n)} z + A_n(\tau), \tag{4.8}$$

$$\text{Re} \left\{ \frac{dz}{d\tau} i\bar{z}_s \right\} = \text{Re} \left\{ (-f(z, \tau) + \overline{zf'(z, \tau)} + \overline{g'(z, \tau)}) i\bar{z}_s \right\}, \tag{4.9}$$

where  $z_s = dz/ds$  denotes the derivative with respect to arclength  $s$  of the boundary  $z(s)$ . The set of functions  $\{A_n(\tau) \mid n = 0, \dots, M\}$  arises from an integration with respect to arclength on each boundary and must be found as part of the cross-plane solution.

The system (4.1) and (4.2) is a highly nonlinear two-dimensional free-boundary problem. Remarkably, several exact solutions to it are known for special geometries (Hopper 1990; Richardson 1992; Tanveer & Vasconcelos 1995; Cummings, Howison & King 1999; Crowdy 2003a,b). Numerical methods must be used, however, for general initial conditions. One option is to make use of standard boundary integral methods (Pozrikidis 1992; Chakravarthy & Chiu 2009), but we eschew this approach in favour of one based on a conformal mapping representation of the boundaries. One reason is that the boundary integral formulation for compressible bubbles, with changing area, suffers from certain technical difficulties involving the appearance of hypersingular integrals in the standard formulation (Pozrikidis 2001, 2003); a second reason is that it is precisely such conformal mapping formulations that give rise to the known exact solutions mentioned above, in particular those for compressible bubbles given by Crowdy (2003a) and which lie at the heart of the model to be described in § 5.

4.1. Numerical method

To track the fluid boundaries in the cross-plane we introduce a  $\tau$ -dependent conformal mapping  $z(\zeta, \tau)$  from a canonical circular region in a complex  $\zeta$ -plane to the evolving fluid region. This canonical preimage region is inside the circle  $|\zeta - \delta_0(\tau)| = q_0(\tau)$  but outside the circles  $|\zeta - \delta_n(\tau)| = q_n(\tau)$  ( $n = 1, \dots, M$ ), where the circle centres  $\delta_n(\tau) \in \mathbb{C}$  and radii  $q_n(\tau) \in \mathbb{R}$  evolve in time. For convenience, we take  $\delta_0(\tau) = 0$  and  $q_0(\tau) = 1$ . The conformal mapping can be represented in general as

$$z(\zeta, \tau) = \sum_{n=0}^M \sum_k a_k^{(n)}(\tau) \left( \frac{\zeta - \delta_n(\tau)}{q_n(\tau)} \right)^k, \tag{4.10}$$

where for the outer boundary ( $n = 0$ ) we take  $k = 0, \dots, \infty$ , while for the inner boundaries ( $n = 1, \dots, M$ ) we take  $k = -1, \dots, -\infty$ . The coefficients  $\{a_k^{(n)}(\tau)\}$  as well as the parameters  $\{\delta_n(\tau), q_n(\tau) \mid n = 1, \dots, M\}$  characterising the preimage circles must be found. With the introduction of this conformal mapping we can now define the composed functions

$$F(\zeta, \tau) \equiv f(z(\zeta, \tau), \tau), \quad G(\zeta, \tau) \equiv g'(z(\zeta, \tau), \tau), \tag{4.11a,b}$$

which are determined, at each  $\tau$  value, by the stress boundary condition (4.8) provided that some additional degrees of freedom are chosen correctly (Buchak & Crowdy 2014). Once  $F(\zeta, \tau)$  and  $G(\zeta, \tau)$  are known, the normal velocity of the boundary can be computed from the kinematic condition (4.9) and the boundary position updated in  $\tau$  using a fourth-order Runge–Kutta scheme. A detailed explanation and performance evaluation of this numerical spectral method for computing the cross-plane evolution will be given elsewhere (Buchak & Crowdy 2014).

To validate the numerical method, we checked it against known analytical solutions for the two-dimensional sintering of  $N$  equal circular cylinders arranged in a doubly connected annular arrangement (Crowdy 2003b). We also verified that our method successfully captures the evolution of a thin viscida of fluid, as predicted by a set of asymptotic equations derived by Griffiths & Howell (2007).

The numerical scheme just described can, in principle, be used to solve the cross-plane problem for any given initial geometry. Here, however, we use it only to test the validity and accuracy of the model introduced in the next section.

5. The elliptical pore model

How can we find initial geometries that, under suitable draw conditions, will produce an MOF with the desired target geometry? Previous authors (Yarin 1995; Griffiths & Howell 2007, 2008) and the present authors (Stokes *et al.* 2014) have addressed this question for special geometries, but it is desirable to be able to handle more general geometries relevant to MOF applications.

Since this is clearly an inverse problem, one option is to consider running the two-dimensional free-surface Stokes flow problem backwards in time, starting with the desired configuration, with the hope of backing out an appropriate initial geometry. However, a little consideration reveals that this inverse problem is ill-posed: surface tension smoothes out ripples in an interface so, in reverse time, any numerical method will be subject to contamination by the growth of initially small numerical inaccuracies. The authors have given a concrete illustrative example of this ill-posedness (Stokes *et al.* 2014); Yarin (1995) has remarked that ‘computers

are practically useless in solving such problems'. Griffiths & Howell (2008, 2009) have acknowledged the difficulty of a backwards-time calculation. It is therefore crucial, in order to solve this inverse problem in any meaningful way, to strategically constrain the class of possible solutions by adding additional information on the type of initial condition one seeks.

Yarin (1995) found that truncation of a Fourier series provided the necessary constraint for solving the inverse problems there considered. Griffiths & Howell (2008, 2009), in their consideration of the drawing of thin-walled non-axisymmetric tubes, presented an asymptotic model of the evolution of their cross-plane geometries which allows the solution to the cross-plane problem to be written down in analytical form by, in essence, tracking only the centreline of a thin viscida. This approach has the subsidiary – and highly desirable – advantage that time can be reversed in a stable manner and predictions made as to initial conditions giving rise to required end-state geometries. In our own prior work (Stokes *et al.* 2014) we made use of various known exact solutions of the cross-plane problem for axisymmetric and non-axisymmetric tubes (of arbitrary wall thickness) to isolate solutions of this inverse problem.

For the geometries typically associated with multichannel MOFs, the models described above cannot be applied. Therefore, we now present a different asymptotic model of the cross-plane flow which we have found to be suited to broad classes of multichannel MOF geometries. The model affords us similar advantages to the models of Griffiths & Howell (2008) and Stokes *et al.* (2014) in that it admits an analytic formulation (thereby obviating the need for a full numerical simulation of the kind expounded in §4) and it can be run backwards in time in a stable manner to give predictions for initial conditions giving rise to the required MOF geometries at the end of the draw.

The main idea is to employ a so-called elliptical pore model (henceforth, EPM) of two-dimensional interacting bubbles in two-dimensional Stokes flows expounded earlier, and in a different context, by one of the authors (Crowdy 2004). The basis of the EPM rests on the mathematical observation (Crowdy 2003a) that an isolated compressible elliptical bubble (or ‘pore’) in a general time-dependent linear Stokes flow remains precisely elliptical in shape under evolution according to the Stokes equations. Given this surprising fact, it was proposed (Crowdy 2004) to model multibubble interactions – in the spirit of inner–outer matched asymptotic expansions – by assuming that, in a far-field sense, each compressible bubble which is generally shrinking under the effects of surface tension will be well modelled as an effective point sink centred at its centroid. Hence, provided that all bubbles are sufficiently far apart (relative to a typical length scale of the bubbles), any given bubble will evolve as an elliptical bubble in the time-dependent irrotational linear strain produced by the superposition of point sinks representing the flow induced by its neighbours. Numerical evidence given by Crowdy (2004) confirmed that this model gives good agreement with the full dynamical evolution of certain test cases.

### 5.1. *Generalised EPM*

The original EPM of Crowdy (2004) proposed to treat the pores, at long-range distances, as pure point sinks in an unbounded region. For MOFs we need to extend this model in two ways. First, to more accurately model the channel interactions, we include contributions from another type of Stokes flow singularity – the stresslet (Pozrikidis 1992) – which we describe below. Second, the bounded geometry of an

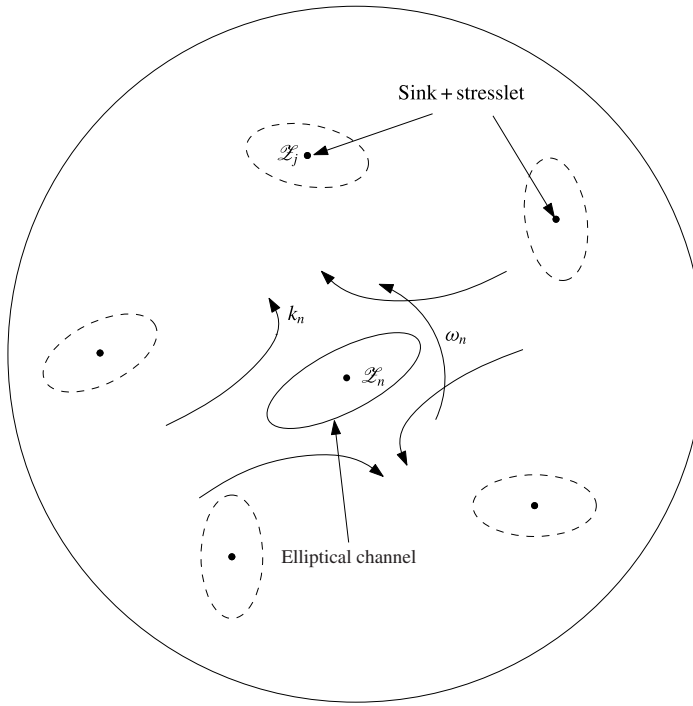


FIGURE 4. Schematic illustrating the idea of the generalised EPM. Each channel, labelled by  $n$ , in the fibre cross-section is modelled as an elliptical bubble in an ambient flow characterised by a local strain rate  $k_n$ , vorticity  $\omega_n$  and pressure  $p_n$  (not shown). This local flow is induced by the other channels and the outer boundary, assumed to be well separated from channel  $n$ .

MOF cross-section requires us to incorporate the effects of an outer boundary in our model.

The components of our model are sketched in figure 4. The cross-section of an MOF is characterised by  $M$  elliptical channels with centroids located at  $\mathcal{L}_n(\tau) \in \mathbb{C}$  ( $n = 1 \dots M$ ) in the cross-plane. We assume that the outer boundary begins and stays circular and centred at the origin as it evolves – an assumption consistent with many MOF geometries used in practice which often comprise rotationally symmetric arrays of channels. Hence, the outer boundary can be described by

$$|z| = R(\tau), \quad (5.1)$$

for some radius  $R(\tau)$  to be determined.

Each channel is modelled, in its far field, as the combination of a source of strength  $m_n(\tau)$  and a stresslet of strength  $\lambda_n(\tau)$ ; note that it is easily shown that the net force on the fluid due to the presence of the channel is zero, thereby precluding any use of Stokeslet singularities to model them. In terms of the Goursat functions introduced in (4.4), a point source/sink of strength  $m_n$  at  $\mathcal{L}_n$  is represented as

$$f(z, \tau) = 0, \quad g'(z, \tau) = \frac{m_n}{2\pi(z - \mathcal{L}_n)}, \quad (5.2a,b)$$

which, from formula (4.6), gives the velocity field

$$u + iv = \frac{m_n}{2\pi(z - \mathcal{Z}_n)}. \tag{5.3}$$

A point stresslet of strength  $\lambda_n$  is represented as

$$f(z, \tau) = \frac{\lambda_n}{2\pi(z - \mathcal{Z}_n)}, \quad g'(z, \tau) = \frac{\lambda_n \overline{\mathcal{Z}_n}}{2\pi(z - \mathcal{Z}_n)^2}, \tag{5.4a,b}$$

which produces the velocity field

$$u + iv = -\frac{\lambda_n}{2\pi(z - \mathcal{Z}_n)} - \frac{\overline{\lambda_n}(z - \mathcal{Z}_n)}{2\pi(z - \mathcal{Z}_n)^2}. \tag{5.5}$$

We have not found this complex variable form of the stresslet singularity documented in the standard textbook literature, but it has been used previously by one of the authors (Crowdy & Or 2010) in modelling low-Reynolds-number swimmers near walls. Together,  $f(z, \tau)$  and  $g'(z, \tau)$  give a velocity field that decays like  $|z|^{-1}$  in the far field. Since the channels generally shrink in size, we expect  $m_n < 0$ . The stresslet strengths  $\lambda_n(\tau)$  are generally complex quantities (reflecting an amplitude and orientation).

The scalings for lengths, velocities and pressures are the same as in §4. To keep the formulation of the model as general as possible, we allow each channel to be pressurised with a given pressure  $p_B^{(n)}(\tau)$ , and use  $p_B^{(0)}(\tau)$  to denote the ambient pressure exterior to the fibre. For the specific purposes of the present paper, however, we later choose  $p_B^{(n)}(\tau) = 0$  for  $n = 0, \dots, M$  (pressurisation effects are studied separately in a forthcoming paper (Chen *et al.* 2015)).

### 5.2. Global flow

The EPM assumes the large-scale description of the flow to be given by (4.4) with

$$f(z, \tau) = \underbrace{\sum_{n=1}^M \frac{\lambda_n(\tau)}{2\pi(z - \mathcal{Z}_n(\tau))}}_{\text{stresslets}} + \underbrace{\frac{1}{4}P(\tau)z}_{\text{outer boundary effect}}, \tag{5.6}$$

$$g'(z, \tau) = \underbrace{\sum_{n=1}^M \frac{m_n(\tau)}{2\pi(z - \mathcal{Z}_n(\tau))}}_{\text{sinks}} + \underbrace{\sum_{n=1}^M \frac{\lambda_n(\tau) \overline{\mathcal{Z}_n(\tau)}}{2\pi(z - \mathcal{Z}_n(\tau))^2}}_{\text{stresslets}}. \tag{5.7}$$

The values of  $m_n$  and  $\lambda_n$  are determined below by considering the evolution of each individual channel. The original EPM formulation of Crowdy (2004) contained only the sink terms labelled in (5.7), but inclusion of the additional stresslet terms in (5.6) and (5.7) means that all physically admissible singularities with velocities decaying like  $|z|^{-1}$  are now incorporated into the model. Because the cross-section of an MOF is a bounded region, the term for the uniform pressure in (5.6) is required to account for the influence of the outer boundary on the inner channels.

5.3. *Outer boundary evolution*

For the flow described by (5.6) and (5.7), the dynamic (4.8) and kinematic (4.9) boundary conditions on the outer boundary give respectively

$$P(\tau) - p_B^{(0)} + \frac{\mathcal{M}}{\pi R^2} = \frac{1}{R}, \tag{5.8}$$

$$\frac{dR}{d\tau} = \frac{\mathcal{M}}{2\pi R}, \tag{5.9}$$

where

$$\mathcal{M} = \sum_{n=1}^M m_n \tag{5.10}$$

is the combined sink strength of the channels and where, for consistency with the assumption of a purely circular outer boundary, we need

$$\frac{1}{R} \sum_{n=1}^M \lambda_n = 0. \tag{5.11}$$

The latter condition is certainly expected to be satisfied by MOFs of practical relevance, involving rotationally symmetric arrays of channels (the modelling of more complicated outer boundary shapes is reserved as a topic for further investigation). Equation (5.8) relates a ‘bulk pressure’  $P(\tau)$  to the ambient pressure  $p_B^{(0)}(\tau)$ , while (5.9) gives the evolution of the outer boundary. These equations are equivalent to modelling the effect of the channels on the outer boundary as a point source/sink of strength  $\mathcal{M}(\tau)$  situated at the centre of the outer boundary circle. In turn, the internal channels feel the effect of the outer boundary through a time varying bulk pressure  $P(\tau)$  coupled to the outer boundary motion through (5.8).

Equations (5.8)–(5.11) are derived in detail in appendix A.

5.4. *Evolution of channels*

To determine how the elliptical channels evolve, we must resolve local details of the flow. Following Crowdy (2004), the evolution of channel  $n$  can be approximated by studying the local field near  $\mathcal{Z}_n$ . Taylor expansion of (5.6) and (5.7) produces

$$\left. \begin{aligned} f(z) &= \left( \frac{1}{4}P\mathcal{Z}_n + \sum_{j \neq n} \frac{\lambda_j}{2\pi(\mathcal{Z}_n - \mathcal{Z}_j)} \right) + \left( \frac{1}{4}P - \sum_{j \neq n} \frac{\lambda_j}{2\pi(\mathcal{Z}_n - \mathcal{Z}_j)^2} \right) (z - \mathcal{Z}_n) \\ &\quad + \left( \sum_{j \neq n} \frac{\lambda_j}{2\pi(\mathcal{Z}_n - \mathcal{Z}_j)^3} \right) (z - \mathcal{Z}_n)^2 + \dots, \\ g'(z) &= \left( \sum_{j \neq n} \frac{m_j}{2\pi(\mathcal{Z}_n - \mathcal{Z}_j)} + \sum_{j \neq n} \frac{\lambda_j \overline{\mathcal{Z}_j}}{2\pi(\mathcal{Z}_n - \mathcal{Z}_j)^2} \right) \\ &\quad + \left( - \sum_{j \neq n} \frac{m_j}{2\pi(\mathcal{Z}_n - \mathcal{Z}_j)^2} - \sum_{j \neq n} \frac{\lambda_j \overline{\mathcal{Z}_j}}{\pi(\mathcal{Z}_n - \mathcal{Z}_j)^3} \right) (z - \mathcal{Z}_n) + \dots \end{aligned} \right\} \tag{5.12}$$

A local expansion of the complex velocity  $u + iv$  about the centre  $\mathcal{Z}_n$  of the  $n$ th channel can then be determined from (4.6). The velocity of the channel centroid is given by the constant term in this expansion,

$$\frac{d\mathcal{Z}_n}{d\tau} = \overline{u(\mathcal{Z}_n)} = - \sum_{j \neq n} \frac{\lambda_j \overline{(\mathcal{Z}_n - \mathcal{Z}_j)}}{2\pi(\mathcal{Z}_n - \mathcal{Z}_j)^2} + \sum_{j \neq n} \frac{m_j}{2\pi(\mathcal{Z}_n - \mathcal{Z}_j)} - \overline{\sum_{j \neq n} \frac{\lambda_j}{2\pi(\mathcal{Z}_n - \mathcal{Z}_j)}}. \quad (5.13)$$

The linear terms in the expansions of  $f(z)$  and  $g'(z)$ , with the origin moved to  $\mathcal{Z}_n$ , determine how the  $n$ th channel shape evolves. A simple calculation leads to

$$\frac{1}{4}(p_n - i\omega_n) = \frac{1}{4}P - \sum_{j \neq n} \frac{\lambda_j}{2\pi(\mathcal{Z}_n - \mathcal{Z}_j)^2}, \quad (5.14)$$

$$k_n = - \sum_{j \neq n} \frac{m_j}{2\pi(\mathcal{Z}_n - \mathcal{Z}_j)^2} - \sum_{j \neq n} \frac{\lambda_j \overline{(\mathcal{Z}_j - \mathcal{Z}_n)}}{\pi(\mathcal{Z}_n - \mathcal{Z}_j)^3}, \quad (5.15)$$

giving the ambient pressure, vorticity and linear strain rate ‘seen’ by the  $n$ th channel in its far field. It should be noted that all quantities (5.13)–(5.15) are invariant under a change of origin.

To close the model, we must determine how the shape of the  $n$ th channel evolves in response to the far-field conditions (5.14) and (5.15). Following Crowdy (2004), the elliptical cross-section of the  $n$ th channel is described by a time-dependent conformal mapping  $z_n(\zeta, \tau)$  of a parametric circle  $|\zeta| = 1$ . Each has the form

$$z_n(\zeta, \tau) = \mathcal{Z}_n(\tau) + \frac{\alpha_n(\tau)}{\zeta} + \beta_n(\tau)\zeta, \quad (5.16)$$

where  $\mathcal{Z}_n(\tau)$  is the centroid position while  $\alpha_n(\tau) \in \mathbb{R}$  and  $\beta_n(\tau) \in \mathbb{C}$  are parameters encoding its orientation, area and eccentricity, with  $|\beta_n| < \alpha_n$ . It is easy to check that (5.16) transplants the interior of the unit  $\zeta$ -disc to the exterior of an ellipse. Indeed, if  $a_n$  and  $b_n$  are the semi-major and semi-minor axes of the elliptical cross-section of the channel, then

$$a_n = \alpha_n + |\beta_n|, \quad b_n = \alpha_n - |\beta_n|, \quad (5.17a,b)$$

while its area is

$$\pi a_n b_n = \pi(\alpha_n^2 - |\beta_n|^2). \quad (5.18)$$

The orientation angle of the semi-major axis of the ellipse to the horizontal axis in the cross-plane is  $(1/2) \arg[\beta_n]$ .

The evolution of a compressible elliptical bubble in an ambient linear flow was found in analytical form by Crowdy (2003a) (see also Pozrikidis (2003) for a purely numerical treatment of the same problem). Those results can be applied to the cross-section of an elliptical channel with far-field conditions on  $f(z)$  and  $g(z)$  taken to be

$$f(z) \sim \frac{1}{4}(p_n - p_B^{(n)} - i\omega_n)z + \frac{\lambda_n}{2\pi z} + \dots, \quad (5.19)$$

$$g'(z) \sim k_n z + \frac{m_n}{2\pi z} + \dots, \quad (5.20)$$

where the coefficients  $p_n - i\omega_n$  and  $k_n$  are read off from (5.14) and (5.15). The dynamic and kinematic boundary conditions (4.8) and (4.9) determine the evolution of the parameters  $\alpha_n(\tau)$  and  $\beta_n(\tau)$  (Crowdy 2003a),

$$\frac{\partial \alpha_n}{\partial \tau} = -\alpha_n I_n(0) - \frac{1}{2} \alpha_n (p_n - p_B^{(n)}), \tag{5.21}$$

$$\frac{\partial \beta_n}{\partial \tau} = -\beta_n I_n(0) + \frac{1}{2} \beta_n (p_n - p_B^{(n)}) + 2\bar{k}_n \alpha_n + i\omega_n \beta_n, \tag{5.22}$$

with  $m_n(\tau)$  and  $\lambda_n(\tau)$  for each channel related to  $\alpha_n(\tau)$  and  $\beta_n(\tau)$  by

$$\frac{m_n}{\pi} = \frac{d}{d\tau} (\alpha_n^2 - |\beta_n|^2), \tag{5.23}$$

$$\frac{\lambda_n}{\pi} = \beta_n \frac{\partial \alpha_n}{\partial \tau} - \alpha_n \frac{\partial \beta_n}{\partial \tau} + i\alpha_n \beta_n \omega_n + 2\alpha_n \beta_n I_n(0) - \frac{1}{2} \alpha_n^2 I_n''(0). \tag{5.24}$$

Expressions for  $I_n(0)$  and  $I_n''(0)$  are given in appendix B. It is apparent from (5.23) and (5.24) that the coefficient  $\lambda_n$  may be complex but  $m_n$  must be real, showing that the channel acts like a superposed stresslet and a source/sink, but has no rotlet contribution.

It is natural to ask what the effect would be of expanding  $f(z, t)$  and  $g'(z, t)$  in (5.12), and hence the velocity field, beyond the linear terms included above. In that case, it is no longer true that an initially elliptical channel sitting in such a higher-order, now nonlinear, ambient flow will remain elliptical. However, some important mathematical generalisations can still be made, and this is discussed further in § 10.

It is instructive to point out that, for a single circular channel at the centre of a circular fibre (i.e. a concentric annular tube), the equations just described retrieve exactly the equations for a pressurised annular fibre that one would obtain by a direct analysis of the equations of motion with radial symmetry (that is, without proceeding via a complex variable and conformal mapping formulation). In other words, the EPM is exact in this case, not an approximation. This is shown in detail in appendix C. The EPM can therefore be understood as a generalised system for the case where the cross-plane comprises more than one channel. It is an approximate system in that case, but one that gives excellent agreement with the exact dynamics provided that the channels are well separated and sufficiently far from the other boundary, as we survey in the next section.

## 6. Effectiveness of the EPM

The model just described leads to a reduction of the full nonlinear free-boundary problem to a coupled system of ordinary differential equations governing the evolution of the parameters  $\mathcal{L}_n(\tau)$ ,  $\alpha_n(\tau)$ ,  $\beta_n(\tau)$  and  $R(\tau)$ . A linear system of equations must be solved at each time step in order to calculate the time derivatives of the parameters. Appendix B illustrates how this can be implemented. We have also made available freely downloadable MATLAB scripts (<http://wwwf.imperial.ac.uk/~dgcrowdy/>) for general use; these scripts carry out the prescription given in appendix B.

Henceforth we impose zero channel pressurisation (3.1). As a first check we verified that the model agreed with a known exact solution for a concentric circular geometry (equations (3.2) of van de Vorst (1993), with  $R_i = 0.5$  and  $R_o = 1$ ).



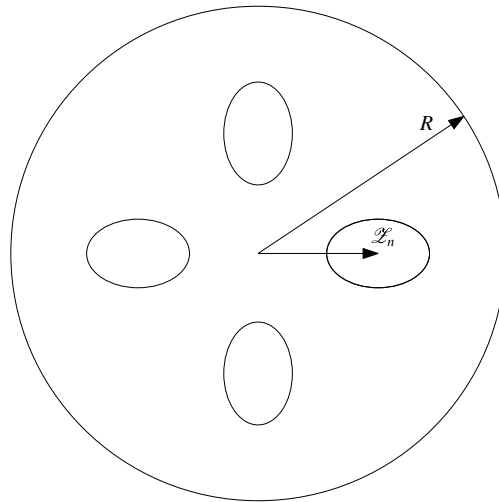


FIGURE 5. The configuration used to test the EPM in figures 6–8. The geometry is characterised by  $M$ , the number of channels, and  $r = |\mathcal{Z}_n|/R$ , the ratio of the radius of the channel centroids to the radius of the outer boundary. Here,  $R$  is chosen so that the fluid region has unit area.

The numerical method of § 4 can be used to test the EPM more generally. We take as a first test configuration the geometry sketched in figure 5, comprising  $M$  elliptical channels characterised by the ratio  $r = |\mathcal{Z}_n|/R$  specifying how close the channels are to the outer boundary. In figure 6, we compare our model with the full solution for a hypothetical MOF whose preform is given by this geometry. (The initial map from a circular domain to the initial configuration is obtained using an extension of the method of Fornberg (1980) developed by Kropf (2009).) Although surface tension causes the shape and size of the channels to change, it is apparent that they remain nearly elliptical in shape. It is also evident that the EPM accurately predicts the time evolution of these ellipses.

Quantitative measures of the accuracy of the EPM are shown in figures 7, 8, where we plot various quantities associated with one of the channels for the test configuration. The agreement is best when the channels are not too close to each other, or to the outer boundary, which is to be expected given the nature of our approximations.

In figure 9, we illustrate the accuracy of the EPM for a hexagonal array, a more realistic geometry for an MOF. In this example, differential straining in the cross-plane leads to certain channels becoming more eccentric than others. In particular, the channels along the innermost ring tend to become extended along the azimuthal direction, while those at the corners of the hexagon on the outermost ring become extended radially. The channels remain roughly elliptical under evolution, and their movement and deformation are captured well by the EPM. This figure shows that the agreement between the model and the full solution is good for a realistic MOF.

## 7. Preliminary experimental validation of the EPM

The authors are currently engaged in a suite of experimental fabrication runs aimed at testing the scope of the mathematical models presented here and in our

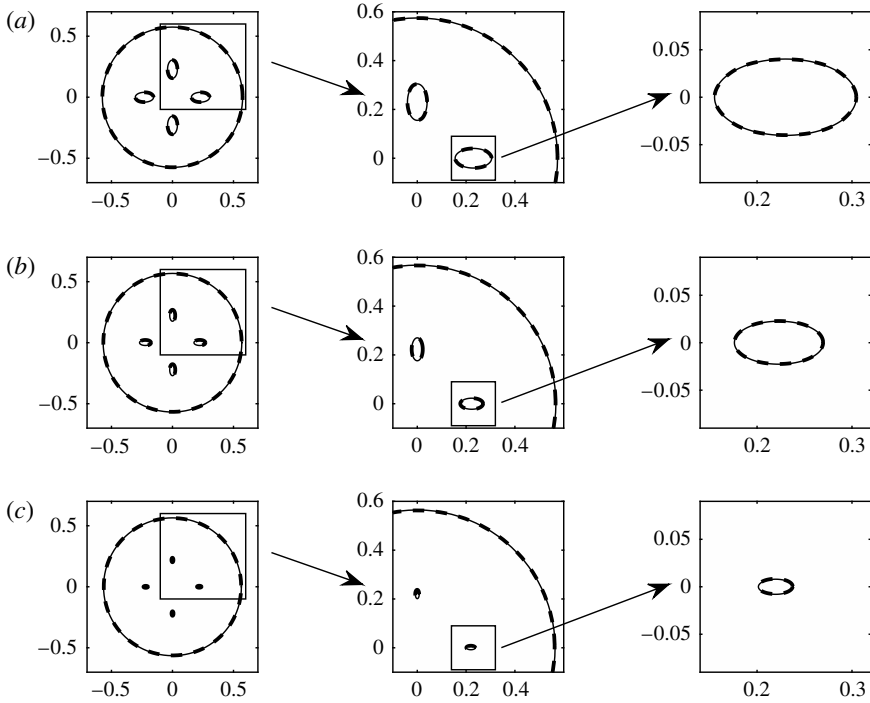


FIGURE 6. Snapshots of the initial configuration (a) and two later configurations (b,c) of an MOF whose initial geometry is shown in figure 5, with  $M=4$  and  $r=0.4$ : (a)  $\tau=0$ , (b)  $\tau=0.040$ , (c)  $\tau=0.080$ . The solid lines show the evolution according to the EPM; the superposed dashed lines are the full solution using the method of § 4. The middle and right-hand columns show close-ups at each time.

related modelling work (Stokes *et al.* 2014; Chen *et al.* 2015). Full details of those results will be presented elsewhere, but it is appropriate to include here preliminary experimental evidence that the EPM (and future variants thereof) has the potential to faithfully predict the kind of qualitative deformations seen in real fibre draws.

For our tests, we chose a preform consisting of six circular channels arranged in a triangle with a circular outer boundary. This configuration is shown in figure 10(a), along with the predicted configurations at  $\tau=0.025, 0.050$  and  $0.075$  in figure 10(b–d). This same initial configuration was used for an experiment, with six holes of diameter 2.8 mm being drilled into an F2 glass cylinder with an outer diameter of 30 mm. The resulting preform was then drawn into fibre using a fixed feed speed and various tensions and draw speeds. Photographs of the cross-section of the fibre were taken for each set of draw parameters. Two photographs, corresponding to two different choices of the draw parameters, are shown in figure 10(e,f).

The qualitative agreement is generally good, although it should be noted that, in the second experimental cross-section, the channels close to the centre are larger than those nearer the edge. This may be due to self-pressurisation, perhaps compounded by a radial temperature gradient; neither of these possibilities has been incorporated into our model. Although not a quantitative test, the agreement shows that the overall channel deformation characteristics predicted by the model are also

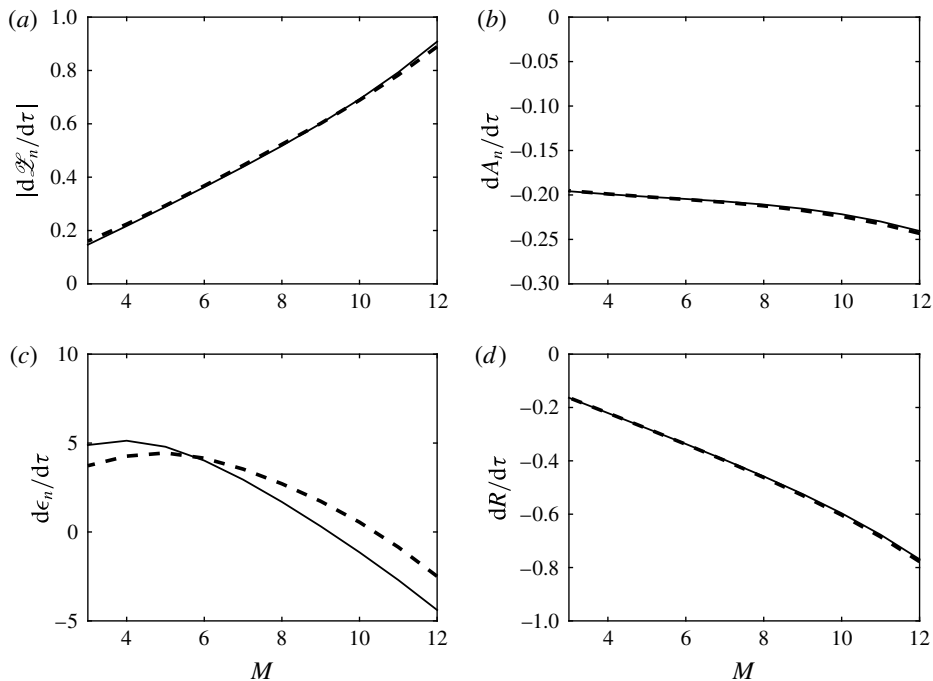


FIGURE 7. Testing the accuracy of the model. Instantaneous rates of change of the centroid location (more precisely, its modulus), area  $A$ , ratio  $\epsilon$  of major to minor axes of a channel and radius of the outer boundary for the MOF illustrated in figure 5, as the number of channels  $M$  is varied, for  $r = |\mathcal{L}_n|/R = 0.4$ . The solid lines show the value of each quantity according to the EPM; the dashed lines show the value obtained from the full numerical solution. The agreement between the EPM and the full solution is best when  $M$  is moderate, that is, when the channels are not too close to each other.

obtained experimentally in fibre drawing, giving confidence in our modelling approach. Quantitative comparisons between the model and experiment are part of ongoing work to be reported in the future.

## 8. The scope of the EPM

The EPM is only technically valid when the channels are well separated and sufficiently far from the outer boundary, but we have found that its predictions compare favourably with a full numerical solution even for channels that are so close together that the underlying asymptotic separation of ‘inner’ and ‘outer’ scales is not expected to pertain. However, in such cases, we have also observed that the EPM needs to be used carefully. For configurations of a large number of close-together channels, we discovered during our test runs that the linear system for the time derivatives of the channel parameters (given in appendix B) can become singular, with a rank deficiency of 1. When this occurs during a simulation, the vector of parameters describing the instantaneous configuration can change by an arbitrary amount in a certain direction (the nullspace direction). An example of such a singular configuration is shown in figure 11(a), with an example of how it can suddenly reconfigure in figure 11(b). We do not understand the reason for this singularity, but it is important to emphasise that the singularity is not real – we have confirmed

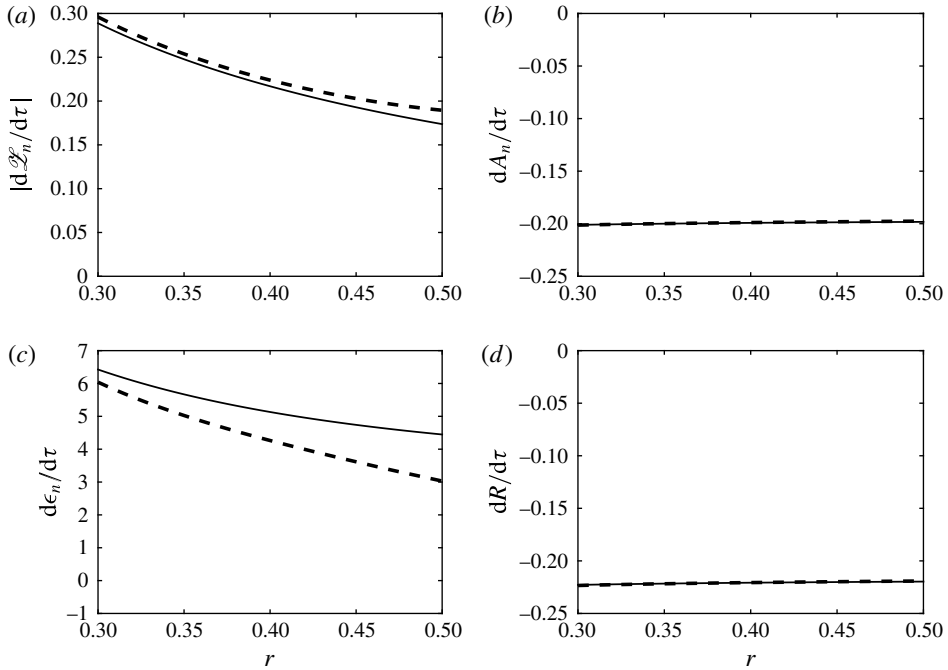


FIGURE 8. Instantaneous rates of change of the quantities plotted in figure 7 as  $r = |\mathcal{Z}_n|/R$  is varied, for  $M = 4$  channels: (a) centroid location, (b) area, (c) axis ratio, (d) outer boundary radius. The solid lines show the value of each quantity according to the EPM; the dashed lines show the value obtained from the full numerical solution. The agreement between the EPM and the full solution is best when  $r$  is small, that is, when the channels are far from the outer boundary.

that nothing similar occurs in the full numerical simulations – but, rather, it is an artefact of the approximations made in the EPM when it is used outside of its range of validity.

This singularity appears to occur in a variety of geometries with a large number of channels whenever the channels are sufficiently close together. It does not appear to be possible to identify in advance whether a given initial configuration will become singular. Because of this, when applying the EPM to geometries with close-together channels, we recommend that the EPM solution be checked to ensure that a singularity has not been crossed. One option is to check the time derivatives for any sudden jumps. Alternatively, the simulation can be run from the final configuration with time reversed and the result compared with the initial configuration. If using a fixed time step, it should be small enough to ensure that the singularity has not been skipped over.

In summary, the EPM agrees well with full numerical simulation within its domain of validity, with identifiable problems occurring outside it. The EPM is therefore a reliable, accurate and fast finite-dimensional reduction of the full infinite-dimensional free-boundary problem in the cross-plane.

Several numerical simulations of fibre drawing have appeared in the literature (Xue *et al.* 2005*a,b,c*; Chakravarthy & Chiu 2009), mainly for MOFs having small numbers of channels. Such approaches are computationally expensive for the complex structures typically seen in MOFs. In contrast, the EPM can be readily solved

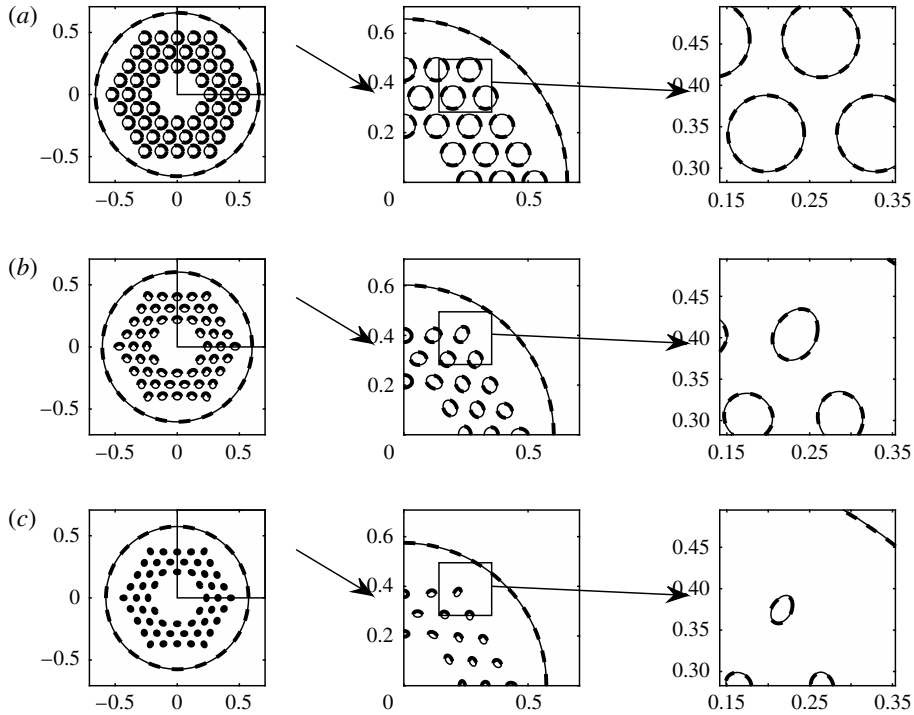


FIGURE 9. Snapshots of the time evolution of an MOF obtained using the EPM (solid lines) and using the numerical method (dashed lines): (a)  $\tau = 0$ , (b)  $\tau = 0.025$ , (c)  $\tau = 0.050$ . The middle and right-hand columns show close-ups at each time.

without the need for effecting a full numerical simulation. This significantly reduces the required computational resources, with the saving becoming more significant, and valuable, as the number of channels increases.

## 9. Regularisation of the inverse problem

Beyond its advantages in reducing the computational demands for the ‘forward problem’, the generalised EPM has a second, arguably more important, advantage: it provides a stable means of finding solutions of the inverse problem discussed earlier. Simply running the full numerical simulation backwards in time rapidly leads to the growth of small numerical inaccuracies that pollute the computation and lead to unrealistic initial geometries. The EPM model can, on the other hand, be successfully run backwards in time – at least until the geometry becomes unphysical, usually by dint of overlapping channels. In this way, the EPM generates physically realistic initial profiles that are viable candidates for realisation as an actual preform. The EPM therefore provides a natural physically based ‘regularisation’ of this ill-posed inverse problem. (Mathematically, the EPM provides a rational way of remaining close to a ‘slow manifold’ with polluting higher-order modes filtered out.)

In this section, we illustrate this calculation for several example target geometries. In all examples to follow, we use a surface tension  $\gamma = 0.25 \text{ N m}^{-1}$ , typical for silicate glasses (Boyd *et al.* 2012). Rather than simply fixing a value of the draw ratio  $D$ , we instead fix the outer fibre diameter at the top of the draw to be 1.02 cm

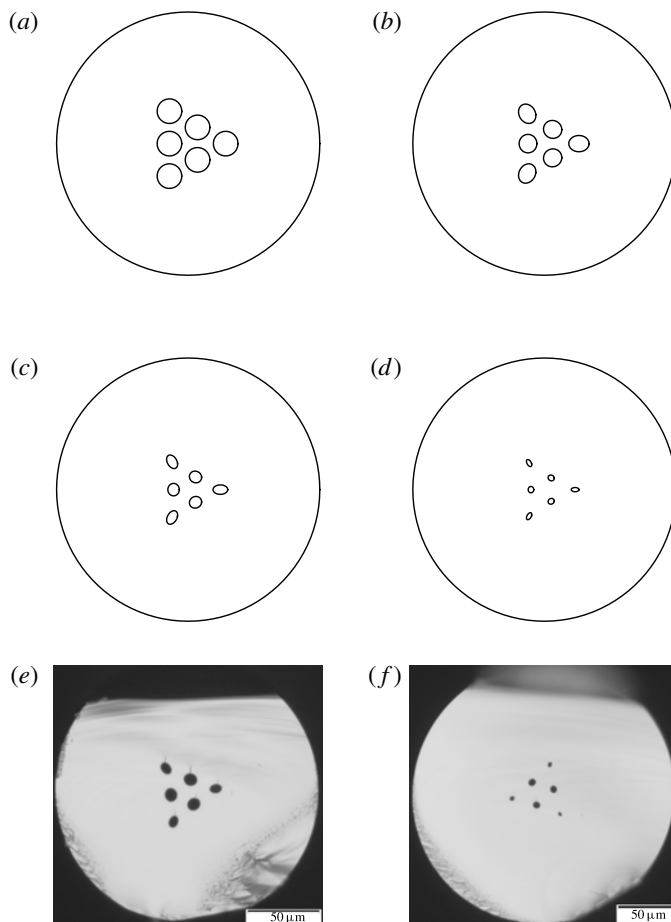


FIGURE 10. Comparison of the EPM with experiment. (a–d) A circular preform with six circular channels (a), and its evolution predicted by the EPM at different times: (a)  $\tau = 0$ , (b)  $\tau = 0.025$ , (c)  $\tau = 0.050$ , (d)  $\tau = 0.075$ . These configurations correspond to possible fibres drawn from this preform. (e,f) Photographs of the fibre cross-section from an experimental draw of a preform with the configuration shown in (a), for two different values of the draw speed and fibre tension. The feed speed was held constant. The scale bars show  $50 \mu\text{m}$ .

and that at the bottom of the draw to be  $160 \mu\text{m}$ ; these are values typically used in real fibre draws. We fix these diameters in order to more closely emulate what is done in practice: the outer diameter at the top of the draw is determined by the preform diameter while the outer diameter at the bottom of the draw is the desired fibre diameter. The draw ratio  $D$  can then be easily calculated from the preform and fibre geometries.

In figures 12(a–d), 13(a–d) and 14(a–f) we pick a target fibre geometry and run the EPM backwards in  $\tau$  time. This allows us to explore possible preform geometries capable of producing this target by picking different values of  $\tau_L$ , i.e. the duration of the EPM calculation. The parameter  $\tau_L$  should be viewed as ‘labelling’ the possible initial geometries. Because the EPM can be run in either direction, the target fibre geometry is recovered by running any of these initial geometries forwards.

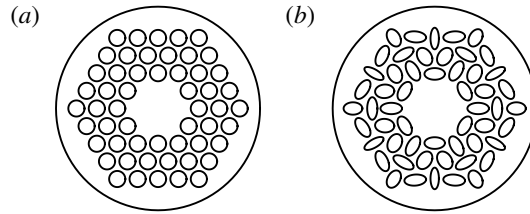


FIGURE 11. The EPM singularity for close-together channels. For the hexagonal array of three rings of channels with channel radii 0.054945 and radial separation 0.138756 (a), the linear system for the time derivatives of the channel parameters is singular. As a result, during a simulation, the configuration can ‘jump’ by an arbitrary multiple of the nullspace (b), which is not physically realistic.

With  $\tau_L$  chosen for each example, both the initial and final geometries are known, and so the draw ratio  $D$  can be calculated. Equations (3.6b) and (3.7) then give the value of the tension  $\sigma$  required for this draw. In figures 12(e,f), 13(e,f) and 14(g,h),  $D$  and  $\sigma$  are plotted as functions of  $\tau_L$ . These are the parameters of interest to experimentalists. Figure 15 shows the profile of the draw for one of the preforms in figure 14.

In these examples, it is evident that the preform configurations corresponding to higher  $\tau_L$  are more different from the target fibre configuration – the channels are larger, closer together and more elliptical, characteristics that might make them more difficult to fabricate. On the other hand, the draw tension  $\sigma$  decreases significantly with increasing  $\tau_L$ , meaning that these configurations would be easier to draw. This suggests that the best choice of initial configuration will be a compromise between a preform that is easy to fabricate and a tension that is easy to achieve.

How well does the EPM solve the inverse problem? Starting with the configuration from figure 14(f), we compared the forward-time evolution of this preform obtained using the EPM with that given by a full numerical simulation. Figure 16 shows snapshots of both. The full numerical simulation gives a final configuration that closely approximates the final EPM configuration, which is the original fibre geometry from figure 14. Thus, the example preform from figure 14 produces a fibre whose channels are at the desired positions and which closely approximate the target circles.

Experimentally, complex preform geometries are becoming easier to achieve with the growing availability of procedures such as the three-dimensional printing of dies (Ebendorff-Heidepriem *et al.* 2014). It is important to remark that the EPM has no theoretical limit on the number of channels – the addition of a new channel simply adds 12 more (real) ordinary differential equations to the system outlined in appendix B.

## 10. Discussion

A reduced model, dubbed the EPM, has been introduced to facilitate fast and accurate simulations of multichannel microstructured optical fibres. Consisting only of a system of ordinary differential equations, the model is ideally suited to MOFs with a large number of channels and, for a wide class of geometries, obviates the need for full numerical simulations.

Significantly, the EPM can also be run backwards in time in a stable manner to give solutions to the inverse problem of predicting the experimental draw parameters and initial preform geometry required to fabricate a chosen target multichannel geometry.

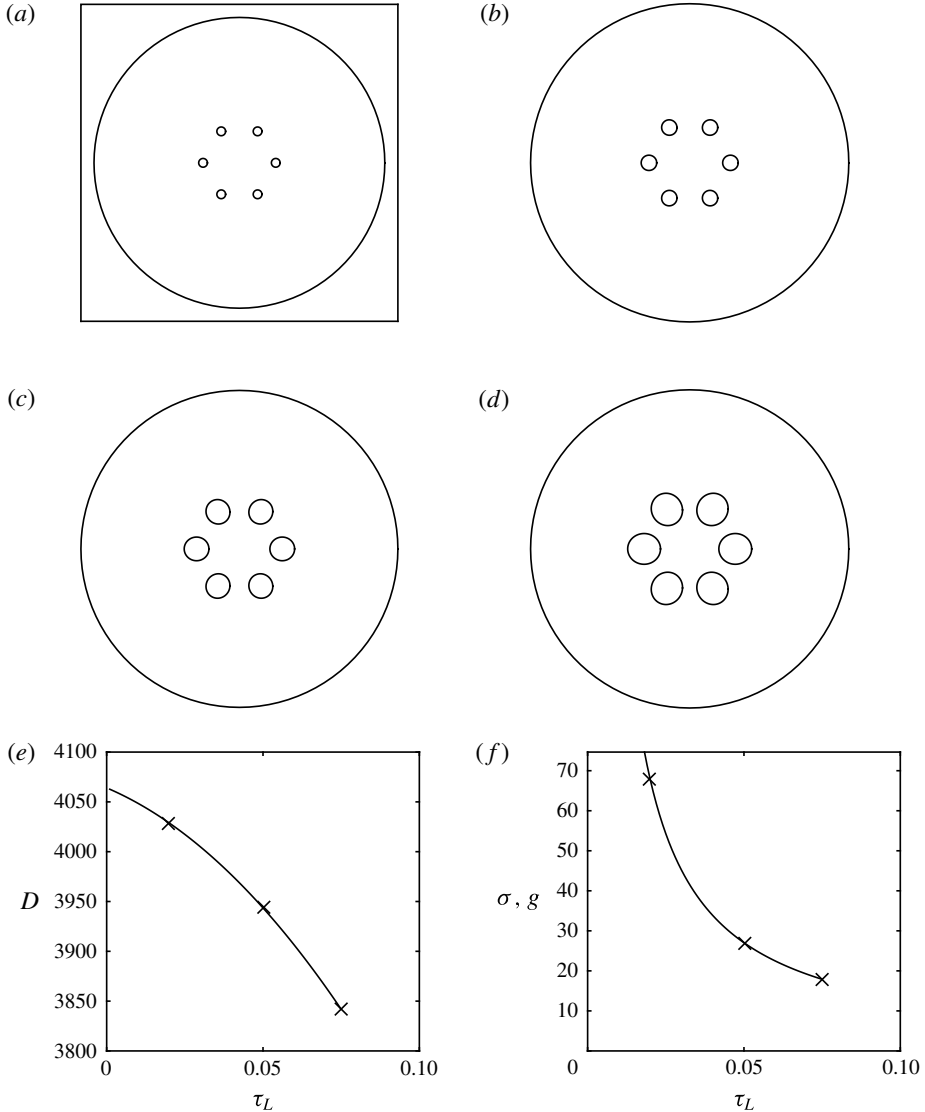


FIGURE 12. Simple fibre geometry with six channels (a), with three example preform geometries that can be used to produce this fibre: (b)  $\tau_L = 0.020$ , (c)  $\tau_L = 0.050$ , (d)  $\tau_L = 0.075$ . Each preform geometry is obtained by starting with the fibre geometry and running the EPM backwards over a time given by  $\tau_L$ . This  $\tau_L$  is the reduced time over which sintering will deform that preform into the desired fibre. (e,f) Values of the draw ratio  $D$  and physical draw tension  $\sigma$  necessary to draw a preform corresponding to  $\tau_L$  into the desired fibre. The values for the examples chosen in the upper plots are marked with crosses.

Mathematically, the EPM provides a means to solve the inverse problem by tracking a relevant slow manifold and filtering off higher modes that would typically pollute a full backwards-time simulation.

One apparent limitation of our modelling approach is the restriction to elliptical channels, but we would like to emphasise that generalisations are possible (and



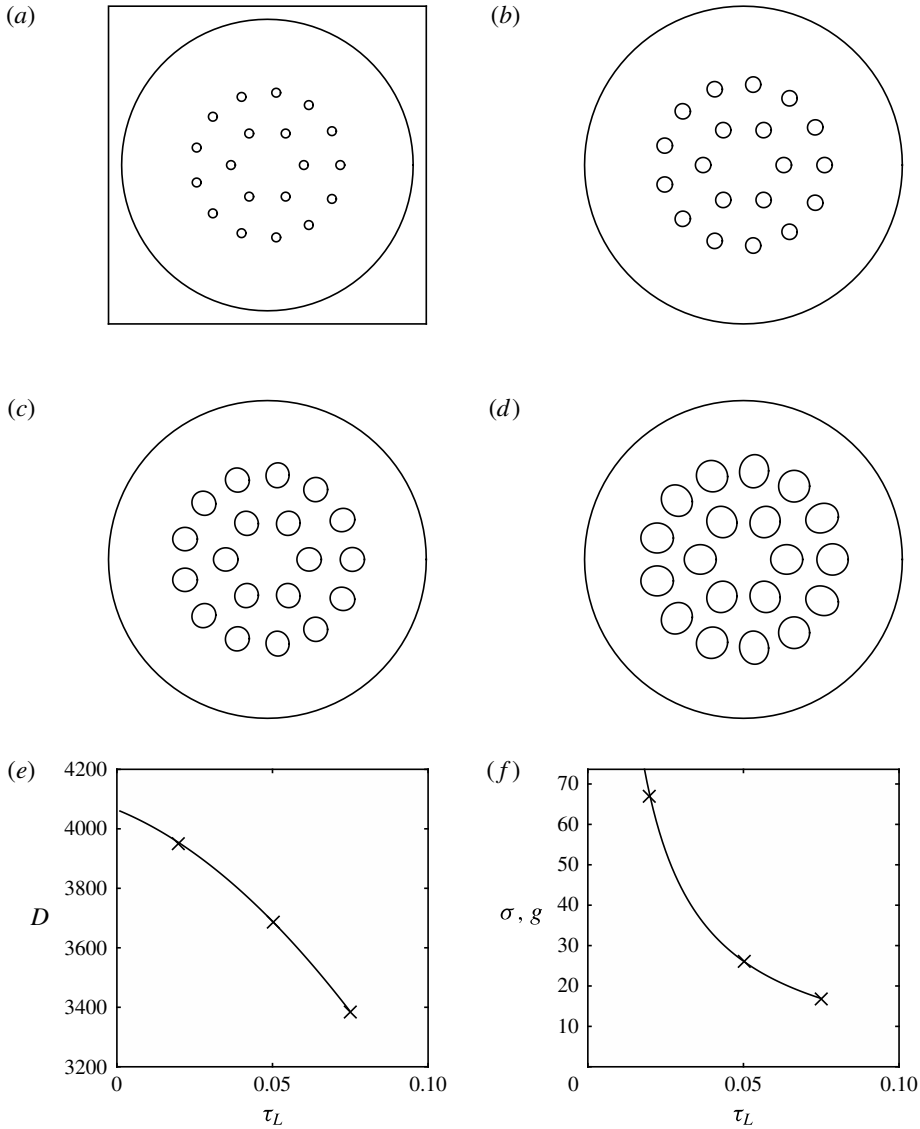


FIGURE 13. A more complicated fibre geometry, with preform geometries calculated by running the EPM backwards in the same manner as in figure 12. The same quantities are plotted.

are under active investigation). The EPM is predicated on the fact, established by Crowdy (2003a), that a compressible elliptical channel – that is, one whose evolving shape is described by a conformal mapping of the form (5.16) – remains elliptical under evolution in a linear Stokes flow. As noted in §7 of Crowdy (2004), similar mathematical features also hold for channels described by generalised conformal mappings of the form

$$z_n(\zeta, \tau) = \mathcal{L}_n(\tau) + \frac{\alpha_n(\tau)}{\zeta} + \beta_n(\tau)\zeta + \dots + \gamma_n(\tau)\zeta^N, \quad (10.1)$$

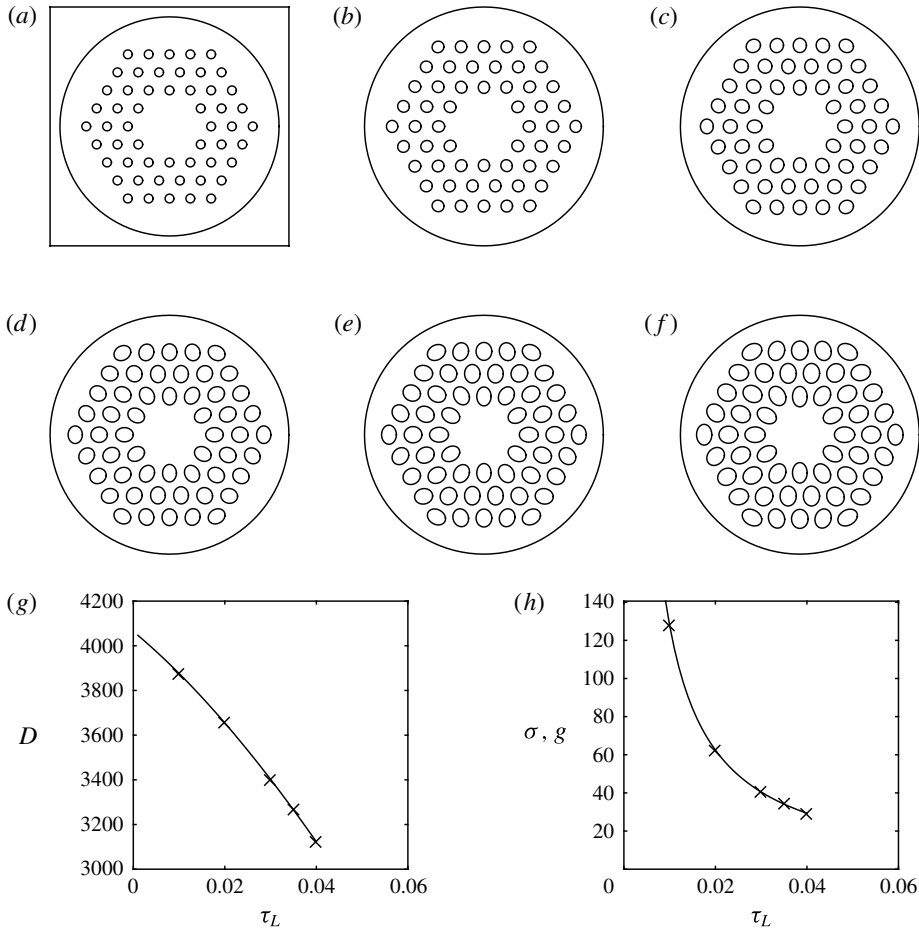


FIGURE 14. A more realistic fibre geometry (a), with preform geometries calculated by running the EPM backwards, like in figures 12 and 13: (b)  $\tau_L = 0.010$ , (c)  $\tau_L = 0.020$ , (d)  $\tau_L = 0.030$ , (e)  $\tau_L = 0.035$ , (f)  $\tau_L = 0.040$ . (g,h) Values of the draw ratio  $D$  and physical draw tension  $\sigma$  necessary to draw a preform corresponding to  $\tau_L$  into the desired fibre. The values for the examples chosen in the upper plots are marked with crosses.

situated in higher-order nonlinear ambient flows. Indeed, based on this idea, Crowdy (2004) modelled the evolution of a doubly periodic array of shrinking channels, which adopt the fourfold rotational symmetry of a square as they close up, and found that it gives excellent agreement with the full numerical boundary integral simulations of Pozrikidis (2003). The EPM is, therefore, just the first in a hierarchy of generalised models in which shapes of more complicated geometrical form can also be simulated (including MOFs with cross-plane geometries comprising arrays of triangular or rectangular channels). Work on extensions of the EPM in this direction will be presented elsewhere.

In practice, pressurisation of the channels is often used as a device to control channel shape evolution. It is therefore important to incorporate such differential channel pressurisation into the model. Work on this is also in progress and will be reported in a forthcoming publication (Chen *et al.* 2015).

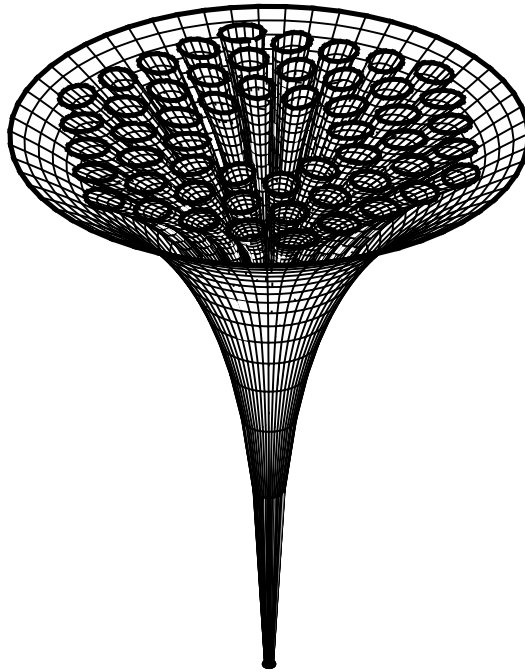


FIGURE 15. The profile of the draw for the preform shown in figure 14(f). The configuration at the bottom is the fibre geometry from figure 14. Equation (3.4) is used to obtain the relation between the reduced time and the axial coordinate, with  $\sigma^*$  obtained by solving (3.6a).

In some circumstances inertia and/or gravity may be of importance, and Cummings & Howell (1999) show that inclusion of these effects modifies only the one-dimensional axial stretching problem, with the two-dimensional cross-plane problem remaining unchanged. Stokes *et al.* (2014) showed that inclusion of inertia prevents the solution from being written in terms of the function  $H(\tau)$ , as in (3.3) and (3.4), but that, even so, the stretching problem is still coupled to the cross-plane problem by the total boundary length, and, for a given preform and surface tension, the final fibre geometry is still determined by the draw ratio and the fibre tension. On inclusion of gravity in the model there is additional fibre tension due to the weight of the fibre hanging below axial position  $x$ , so that the fibre tension is, properly, position-dependent. This makes solution of the stretching problem more complicated, especially as the geometry within the neck-down region will be important, but the coupling to the cross-plane problem remains unchanged. Importantly, with inclusion of inertia and/or gravity, solution of the inverse problem is still dependent on the ability to run the cross-plane problem backwards as done in the present work with both inertia and gravity neglected. Work on inclusion of gravity in the model is in progress and will be reported in a future publication.

Another mechanism sometimes used for control of the fibre draw process is rotation of the fibre during drawing. Besides giving the resulting fibre a twisted geometry (Voyce, Fitt & Monro 2004, 2008), this allows control over channel inflation. Fibre rotation is something we have not yet considered and so remains for future investigation.

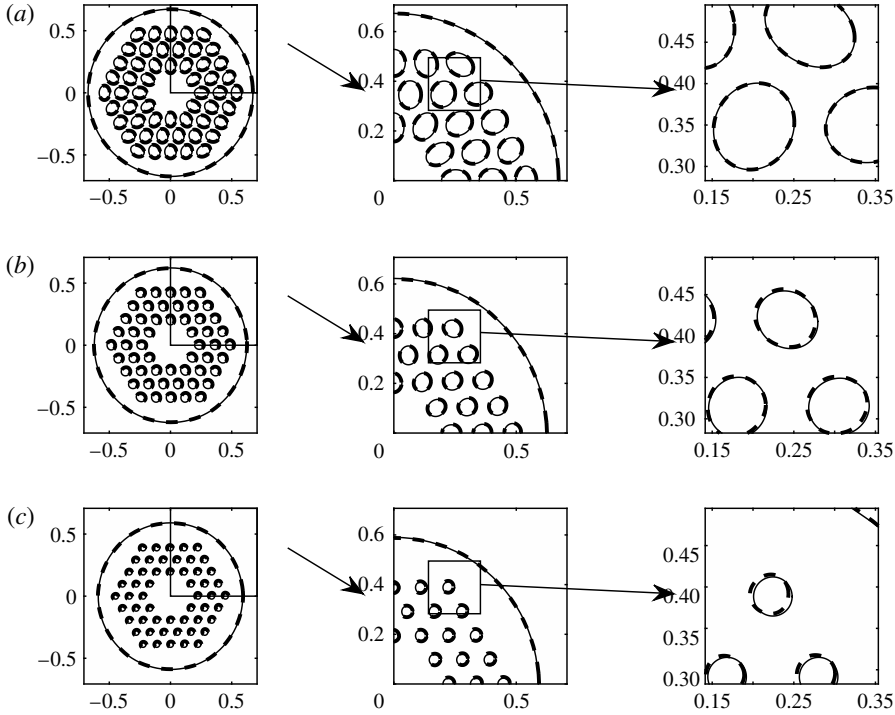


FIGURE 16. Snapshots of the forward-time evolution of the preform shown in figure 14(f) obtained using the EPM (solid lines) and using the numerical method (dashed lines): (a)  $\tau = 0$ , (b)  $\tau = 0.020$ , (c)  $\tau = 0.040$ . The middle and right-hand columns show close-ups at each time.

**Acknowledgements**

D.G.C. acknowledges financial support from Leverhulme Trust Research Grant RPG-358 and an EPSRC Established Career Fellowship. Y.M.S., D.G.C. and H.E.-H. acknowledge support from Research Grant DP130101541 from the Australian Research Council. The work was in part performed at the Optofab node of the Australian National Fabrication Facility utilising Commonwealth and SA State Government funding. We wish to thank A. Dowler and H. Foo at the University of Adelaide for fibre drawing and optical microscopy respectively.

**Appendix A. Derivation of outer boundary evolution**

Here we show that (5.8)–(5.10) follow from our model of a circular outer boundary influenced by a collection of sources and stresslets located near the centre. Starting with a large-scale flow described by

$$f(z, \tau) = \sum_{n=1}^M \frac{\lambda_n}{2\pi(z - \mathcal{L}_n)} + \sum_{n=0}^{\infty} f_n z^n, \tag{A 1}$$

$$g'(z, \tau) = \sum_{n=1}^M \frac{m_n}{2\pi(z - \mathcal{L}_n)} + \sum_{n=1}^M \frac{\lambda_n \overline{\mathcal{L}_n}}{2\pi(z - \mathcal{L}_n)^2} + \sum_{n=0}^{\infty} g_n z^n, \tag{A 2}$$

which is more general than the flow assumed in (5.6) and (5.7), the coefficients of powers of  $z$  are equated in the dynamic boundary condition (4.8) on the outer boundary  $|z| = R$ . To leading order in the quantities  $\mathcal{L}_n/R$ , the equations for  $z^3$ ,  $z^2$ ,  $z^1$ ,  $z^0$  and  $z^{-1}$  are respectively

$$f_3 = \frac{1}{2\pi R^4} \sum_{n=1}^M \bar{\lambda}_n, \tag{A 3}$$

$$f_2 = 0, \tag{A 4}$$

$$f_1 + \bar{f}_1 = \frac{1}{2R} + \frac{1}{2} p_B^{(0)} - \frac{1}{2\pi R^2} \sum_{n=1}^M m_n, \tag{A 5}$$

$$f_0 + 2R^2 \bar{f}_2 + \bar{g}_0 = A_1, \tag{A 6}$$

$$3R^4 \bar{f}_3 + R^2 \bar{g}_1 = -\frac{1}{2\pi} \sum_{n=1}^M \lambda_n, \tag{A 7}$$

where we have made use of the result from (5.23) that the  $m_n$  are real. The equations for  $z^4$  and higher require  $f_4, f_5, \dots = 0$ , while the equations for  $z^{-2}$  and lower require  $g_2, g_3, \dots = 0$ . The degrees of freedom associated with the Goursat description of the flow field and the arbitrary rigid motion of the free-boundary problem may be fixed by setting  $f_0 = 0$ ,  $g_0 = 0$  and  $\text{Im}\{f_1\} = 0$  (Buchak & Crowdy 2014). Defining  $P$  to be the pressure near the centre induced by the outer boundary,

$$P = 4\text{Re}\{f'(0)\} = 4f_1, \tag{A 8}$$

the flow field is

$$f(z, \tau) = \sum_{n=1}^M \frac{\lambda_n}{2\pi(z - \mathcal{L}_n)} + \frac{1}{4} Pz + \frac{1}{2\pi R^4} \left( \sum_{n=1}^M \bar{\lambda}_n \right) z^3, \tag{A 9}$$

$$g'(z, \tau) = \sum_{n=1}^M \frac{m_n}{2\pi(z - \mathcal{L}_n)} + \sum_{n=1}^M \frac{\lambda_n \bar{\mathcal{L}}_n}{2\pi(z - \mathcal{L}_n)^2} - \frac{2}{\pi R^2} \left( \sum_{n=1}^M \bar{\lambda}_n \right) z, \tag{A 10}$$

with  $A_1 = 0$ ,  $P$  given by (5.8) and  $\mathcal{M}$  defined by (5.10). Equating the coefficients of powers of  $z$  in the kinematic boundary condition (4.9), the equation for  $z^0$  gives (5.9), while the equations for  $z^2$  and  $z^{-2}$  both give condition (5.11).

### Appendix B. Implementation of the generalised EPM

The model described in § 5 requires solution of, at each time step, a linear system of complex equations for the first-order time derivatives of  $\mathcal{L}_n$ ,  $\alpha_n$ ,  $\beta_n$  and  $R$ . This linear system is determined by the current values of  $\mathcal{L}_n$ ,  $\alpha_n$ ,  $\beta_n$  and  $R$ . Writing the complex unknowns as a vector  $\mathbf{U}$  of  $5M$  components and the real unknowns as a vector  $\mathbf{V}$  of  $2M + 3$  components,

$$\mathbf{U} = \begin{pmatrix} \dot{\mathcal{L}}_n \\ \dot{\beta}_n \\ p_n - i\omega_n \\ k_n \\ \lambda_n \end{pmatrix}, \quad \mathbf{V} = \begin{pmatrix} \dot{\alpha}_n \\ m_n \\ \dot{R} \\ P \\ \mathcal{M} \end{pmatrix}, \tag{B 1a,b}$$

the system takes the form

$$AU + B\bar{U} + CV = D, \tag{B 2}$$

$$EU + \bar{E}\bar{U} + FV = G, \tag{B 3}$$

where  $A, B, C$  and  $D$  encode the  $5M$  complex equations

$$\begin{pmatrix} \text{equation (5.13)} \\ \text{equation (5.22)} \\ \text{equation (5.14)} \\ \text{equation (5.15)} \\ \text{equation (5.24)} \end{pmatrix} \begin{pmatrix} U \\ V \end{pmatrix} = \begin{pmatrix} \dots \\ \dots \\ \dots \\ \dots \\ \dots \end{pmatrix}, \tag{B 4}$$

and  $E, F$  and  $G$  describe the  $2M + 3$  real equations

$$\begin{pmatrix} \text{equation (5.21)} \\ \text{equation (5.23)} \\ \text{equation (5.8)} \\ \text{equation (5.9)} \\ \text{equation (5.10)} \end{pmatrix} \begin{pmatrix} U \\ V \end{pmatrix} = \begin{pmatrix} \dots \\ \dots \\ \dots \\ \dots \\ \dots \end{pmatrix}. \tag{B 5}$$

We solve this system by rewriting it as a system of real equations for  $\text{Re}\{U\}$ ,  $\text{Im}\{U\}$  and  $V$ . The function  $I_n(\zeta)$ , appearing in (5.21), (5.22) and (5.24), is defined by (2.17) in Crowdy (2003a),

$$I_n(\zeta) = \frac{1}{4\pi i} \oint_{|\zeta'|=1} \frac{d\zeta'}{\zeta'} \left( \frac{\zeta' + \zeta}{\zeta' - \zeta} \right) \frac{1}{|z_{n\zeta}(\zeta')|}. \tag{B 6}$$

Hence,

$$I_n(0) = \frac{1}{4\pi i} \oint_{|\zeta'|=1} \frac{d\zeta'}{\zeta'} \frac{1}{|z_{n\zeta}(\zeta')|}, \quad I_n''(0) = \frac{1}{\pi i} \oint_{|\zeta'|=1} \frac{d\zeta'}{\zeta'^3} \frac{1}{|z_{n\zeta}(\zeta')|}. \tag{B 7a,b}$$

The authors have prepared freely downloadable MATLAB files (<http://wwwf.imperial.ac.uk/~dgcrowdy/>) that compute the evolution of a user-defined initial configuration of channels.

### Appendix C. Governing equations for pressurised annular fibre

Here, we show that, for a single circular channel centred at the origin, the EPM retrieves the exact equations for the cross-plane evolution.

Equations (5.8)–(5.10) give the evolution of the outer boundary, assuming no outer boundary pressure,

$$P + \frac{m_1}{\pi R^2} = \frac{1}{R}, \tag{C 1}$$

$$\frac{dR}{d\tau} = \frac{m_1}{2\pi R}. \tag{C 2}$$

For a single channel with no other channels to interact with, (5.14) and (5.15) give simple expressions for the far-field pressure, vorticity and strain rate,

$$\frac{1}{4}(p_1 - i\omega_1) = \frac{1}{4}P, \tag{C 3}$$

$$k_1 = 0. \tag{C 4}$$

Likewise, (5.13) gives the velocity of the centroid,

$$\frac{d\mathcal{Z}_1}{d\tau} = 0. \tag{C5}$$

Assuming that the channel is initially circular and centred at the origin, it will be described by the map (5.16) with  $\mathcal{Z}_1 = 0$ ,

$$z_1(\zeta, \tau) = \frac{\alpha_1(\tau)}{\zeta} + \beta_1(\tau)\zeta, \tag{C6}$$

with  $\beta_1(0) = 0$ . Equations (5.21) and (5.22) give the evolution of  $\alpha_1(\tau)$  and  $\beta_1(\tau)$ ,

$$\frac{d\alpha_1}{d\tau} = -\alpha_1 I_1(0) - \frac{1}{2}\alpha_1(p_1 - p_B^{(1)}), \tag{C7}$$

$$\frac{d\beta_1}{d\tau} = -\beta_1 I_1(0) + \frac{1}{2}\beta_1(p_1 - p_B^{(1)}) + 2\bar{k}_1\alpha_1 + i\omega_1\beta_1. \tag{C8}$$

Because  $\beta_1(0) = 0$  and  $k_1 = 0$ , it is clear that  $d\beta_1/d\tau = 0$ , so  $\beta_1(\tau) = 0$  and the channel will remain circular for all time. The map  $z_1(\zeta, \tau)$  takes the simpler form

$$z_1(\zeta, \tau) = \frac{\alpha_1(\tau)}{\zeta}. \tag{C9}$$

The integral  $I_1(0)$ , which appears in the equation for  $d\alpha_1/d\tau$ , can be evaluated explicitly for this simple  $z_1(\zeta, \tau)$ ,

$$I_1(0) = \frac{1}{4\pi i} \oint_{|\zeta'|=1} \frac{d\zeta'}{\zeta'} \frac{1}{|z_{n\zeta}(\zeta')|} = \frac{1}{4\pi i} \oint_{|\zeta'|=1} \frac{d\zeta'}{\zeta'} \frac{|\zeta'|^2}{\alpha_1} = \frac{1}{2\alpha_1}. \tag{C10}$$

This gives a simplified equation for  $d\alpha_1/d\tau$ ,

$$\frac{d\alpha_1}{d\tau} = -\frac{1}{2} - \frac{1}{2}\alpha_1(p_1 - p_B^{(1)}). \tag{C11}$$

Finally, with  $\beta_1(\tau) = 0$ , (5.23) gives a simple expression for  $m_1$ ,

$$\frac{m_1}{\pi} = \frac{d}{d\tau}(\alpha_1^2). \tag{C12}$$

Equations (C1)–(C3), (C11) and (C12) can be combined into two equations in the unknowns  $\alpha_1(\tau)$  and  $R(\tau)$ ,

$$\frac{d\alpha_1}{d\tau} = -\frac{1}{2} - \frac{1}{2}\alpha_1 \left( -\frac{1}{R^2} \frac{d}{d\tau}(\alpha_1^2) + \frac{1}{R} - p_B^{(1)} \right), \tag{C13}$$

$$\frac{dR}{d\tau} = \frac{1}{2R} \frac{d}{d\tau}(\alpha_1^2). \tag{C14}$$

Equation (C14) can be rewritten as

$$\frac{d}{d\tau}(R^2) = \frac{d}{d\tau}(\alpha_1^2), \tag{C15}$$

which is just conservation of mass. Since our cross-plane problem has unit fluid area, it integrates to

$$\pi(R^2 - \alpha_1^2) = 1. \quad (\text{C } 16)$$

Now, letting  $\alpha_1 = \rho R$ , (C 13) becomes, after using (C 15) to eliminate  $d(\alpha_1^2)/d\tau$ ,

$$\frac{d\rho}{d\tau} = -\frac{1}{2R}(1 + \rho) + \frac{1}{2}\rho p_B^{(1)}. \quad (\text{C } 17)$$

Equation (C 16) becomes  $\pi R^2(1 - \rho^2) = 1$ . Using this to eliminate  $R$ ,

$$\frac{d\rho}{d\tau} = -\frac{\sqrt{\pi}}{2}(1 + \rho)^{3/2}(1 - \rho)^{1/2} + \frac{1}{2}\rho p_B^{(1)}. \quad (\text{C } 18)$$

Equation (C 18) is derived by direct means in Chen *et al.* (2015), where  $p_B^{(1)} = p_H^* \chi / \gamma^*$ ,  $p_H^*$  being the pressure applied in the channel. For the case of no channel pressurisation,  $p_B^{(1)} = 0$ , it is also readily obtained from equations (4.4a,b) from Stokes *et al.* (2014).

#### REFERENCES

- BOYD, K., EBENDORFF-HEIDEPRIEM, H., MONRO, T. M. & MUNCH, J. 2012 Surface tension and viscosity measurement of optical glasses using a scanning CO<sub>2</sub> laser. *Opt. Mater. Express* **2** (8), 1101–1110.
- BUCHAK, P. & CROWDY, D. G. 2014 Surface-tension-driven Stokes flow: a numerical method based on conformal geometry. *J. Comput. Phys.* (submitted).
- CHAKRAVARTHY, S. S. & CHIU, W. K. S. 2009 Boundary integral method for the evolution of slender viscous fibres containing holes in the cross-section. *J. Fluid Mech.* **621**, 155–182.
- CHEN, M. J., STOKES, Y. M., BUCHAK, P., CROWDY, D. G. & EBENDORFF-HEIDEPRIEM, H. 2015 Microstructured optical fibre drawing with active channel pressurisation. *J. Fluid Mech.* (submitted).
- CHEN, Y. & BIRKS, T. A. 2013 Predicting hole sizes after fibre drawing without knowing the viscosity. *Opt. Mater. Express* **3** (3), 346–356.
- CROWDY, D. G. 2003a Compressible bubbles in Stokes flow. *J. Fluid Mech.* **476**, 345–356.
- CROWDY, D. G. 2003b Viscous sintering of unimodal and bimodal cylindrical packings with shrinking pores. *Eur. J. Appl. Maths* **14**, 421–445.
- CROWDY, D. G. 2004 An elliptical-pore model of late-stage planar viscous sintering. *J. Fluid Mech.* **501**, 251–277.
- CROWDY, D. G. & OR, Y. 2010 Two-dimensional point singularity model of a low-Reynolds-number swimmer near a wall. *Phys. Rev. E* **81**, 036313.
- CUMMINGS, L. & HOWELL, P. D. 1999 On the evolution of non-axisymmetric viscous fibres with surface tension, inertia and gravity. *J. Fluid Mech.* **389**, 361–389.
- CUMMINGS, L., HOWISON, S. & KING, J. R. 1999 Two-dimensional Stokes and Hele-Shaw flow with free surfaces. *Eur. J. Appl. Maths* **10**, 635–680.
- EBENDORFF-HEIDEPRIEM, H., SCHUPPICH, J., DOWLER, A., LIMA-MARQUES, L. & MONRO, T. M. 2014 3D-printed extrusion dies: a versatile approach to optical material processing. *Opt. Mater. Express* **4** (8), 1494–1504.
- FITT, A. D., FURUSAWA, K., MONRO, T. M., PLEASE, C. P. & RICHARDSON, D. A. 2002 The mathematical modelling of capillary drawing for holey fibre manufacture. *J. Engng Maths* **43**, 201–227.
- FORNBERG, B. 1980 A numerical method for conformal mappings. *SIAM J. Sci. Stat. Comput.* **1** (3), 386–400.
- GOSPODINOV, P. & YARIN, A. L. 1997 Draw resonance of optical microcapillaries in non-isothermal drawing. *Intl J. Multiphase Flow* **23**, 967–976.



- GRIFFITHS, I. M. & HOWELL, P. D. 2007 The surface-tension-driven evolution of a two-dimensional annular viscous tube. *J. Fluid Mech.* **593**, 181–208.
- GRIFFITHS, I. M. & HOWELL, P. D. 2008 Mathematical modelling of non-axisymmetric capillary tube drawing. *J. Fluid Mech.* **605**, 181–208.
- GRIFFITHS, I. M. & HOWELL, P. D. 2009 The surface-tension-driven retraction of a viscida. *SIAM J. Appl. Maths* **70** (5), 1453–1487.
- HOPPER, R. W. 1990 Plane Stokes flow driven by capillarity of a free surface. *J. Fluid Mech.* **213**, 349–375.
- ISSA, N. A., VAN EIJKELNBORG, M. A., FELLEW, M., COX, F., HENRY, G. & LARGE, M. C. J. 2004 Fabrication and study of microstructured optical fibers with elliptical holes. *Opt. Lett.* **29** (12), 1336–1338.
- KOSTECKI, R., EBENDORFF-HEIDPRIEM, H., WARREN-SMITH, S. & MONRO, T. 2014 Predicting the drawing conditions for microstructured optical fiber fabrication. *Opt. Mater. Express* **4**, 29–40.
- KROPF, E. 2009 A Fornberg-like method for the numerical conformal mapping of bounded multiply connected domains, Master's thesis, Wichita State University.
- LANGLOIS, W. 1964 *Slow Viscous Flow*. Macmillan.
- LYYTIKÄINEN, K. J. 2004 Control of complex structural geometry in optical fibre drawing, PhD thesis, University of Sydney.
- PEARSON, J. R. A. & MATOVICH, M. A. 1969 Spinning a molten threadline; stability. *Ind. Engng Chem. Fundam.* **8**, 605–609.
- POZRIKIDIS, C. 1992 *Boundary Integral and Singularity Methods for Linearized Viscous Flows*. Cambridge University Press.
- POZRIKIDIS, C. 2001 Expansion of a compressible gas bubble in Stokes flow. *J. Fluid Mech.* **442**, 171–189.
- POZRIKIDIS, C. 2003 Computation of the pressure inside bubbles and pores in Stokes flow. *J. Fluid Mech.* **474**, 319–337.
- RICHARDSON, S. 1992 Two-dimensional slow viscous flows with time-dependent free boundaries driven by surface tension. *Eur. J. Appl. Maths* **3**, 193–207.
- SCHEID, B., QUILGOTTI, S., TRANH, B., GY, R. & STONE, H. A. 2010 On the (de)stabilization of draw resonance due to cooling. *J. Fluid Mech.* **636**, 155–176.
- STOKES, Y. M., BUCHAK, P., CROWDY, D. G. & EBENDORFF-HEIDPRIEM, H. 2014 Drawing of hollow-core fibres: circular and non-circular tubes. *J. Fluid Mech.* **755**, 176–203.
- TANVEER, S. & VASCONCELOS, G. L. 1995 Time-evolving bubbles in two-dimensional Stokes flow. *J. Fluid Mech.* **301**, 325–344.
- TARONI, M., BREWARD, C. J. W., CUMMINGS, L. J. & GRIFFITHS, I. M. 2013 Asymptotic solutions of glass temperature profiles during steady optical fibre drawing. *J. Engng Maths* **80**, 1–20.
- VAN DE VORST, G. A. L. 1993 Integral method for a two-dimensional Stokes flow with shrinking holes applied to viscous sintering. *J. Fluid Mech.* **257**, 667–689.
- VOYCE, C. J., FITT, A. D. & MONRO, T. M. 2004 Mathematical model of the spinning of microstructured fibres. *Opt. Express* **12** (23), 5810–5820.
- VOYCE, C. J., FITT, A. D. & MONRO, T. M. 2008 The mathematical modelling of rotating capillary tubes for holey-fibre manufacture. *J. Engng Maths* **60**, 69–87.
- XUE, S. C., LARGE, M. C. J., BARTON, G. W., TANNER, R. I., POLADIAN, L. & LWIN, R. 2005a Role of material properties and drawing conditions in the fabrication of microstructured optical fibres. *J. Lightwave Technol.* **24**, 853–860.
- XUE, S. C., TANNER, R. I., BARTON, G. W., LWIN, R., LARGE, M. C. J. & POLADIAN, L. 2005b Fabrication of microstructured optical fibres – Part I: problem formulation and numerical modeling of transient draw process. *J. Lightwave Technol.* **23**, 2245–2254.
- XUE, S. C., TANNER, R. I., BARTON, G. W., LWIN, R., LARGE, M. C. J. & POLADIAN, L. 2005c Fabrication of microstructured optical fibres – Part II: numerical modeling of steady-state draw process. *J. Lightwave Technol.* **23**, 2255–2266.

- YARIN, A., RUSINOV, V. I., GOSPODINOV, P. & ST. RADEV 1989 Quasi one-dimensional model of drawing of glass micro capillaries and approximate solutions. *Theor. Appl. Mech.* **20** (3), 55–62.
- YARIN, A. L. 1995 Surface-tension-driven flows at low Reynolds number arising in optoelectronic technology. *J. Fluid Mech.* **286**, 173–200.
- YARIN, A. L., GOSPODINOV, P. & ROUSSINOV, V. I. 1994 Stability loss and sensitivity in hollow fiber drawing. *Phys. Fluids* **6**, 1454–1463.